Supplementary Information

Bipolar membranes reveal surface-hydroxyl-structure-dependent water dissociation mechanism

Huijun Lv[1†], Chao Yang[2†], Minghao Sun[3], Yu Yang[3,4], Fengwang Li[3,4], Pengfei Ou[2]*, Yuhang Wang[1]*

[1]*Institute of Functional Nano & Soft Materials (FUNSOM), Soochow University, 199 Ren'ai Road, Suzhou, Jiangsu, 215123, China*

[2]*Department of Chemistry, National University of Singapore, 3 Science Drive 3, Singapore 117543, Singapore*

[3]*School of Chemical and Biomolecular Engineering, The University of Sydney, Sydney, NSW 2006, Australia*

[4]*ARC Centre of Excellence for Green Electrochemical Transformation of Carbon Dioxide, The University of Sydney, Sydney, NSW 2006, Australia*

[†]*These authors contributed equally: Huijun Lv, Chao Yang*

*Correspondence should be addressed to Pengfei Ou (pengf.ou@nus.edu.sg) and Yuhang Wang (yhwang1988@suda.edu.cn).

The PDF file includes:

Supplementary Figures 1-44
Supplementary Tables 1-7
Supplementary References

Supplementary Figures and Tables.

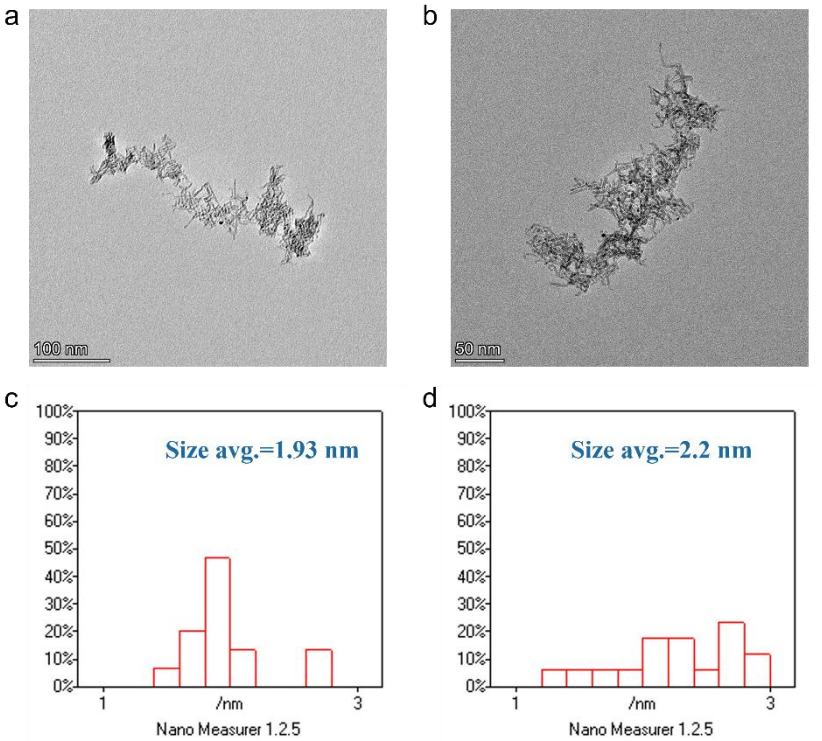

Supplementary Figure 1 | Morphological analysis of SnO_2 quantum wires. High-resolution transmission electron microscopy (HRTEM) images and corresponding particle size distribution histograms of (a, c) QWs4, and (b, d) QWs7. Particle size distributions were extracted from HRTEM images using NanoMeasurer software. The results confirm a progressive increase in average diameter with prolonged solvothermal reaction time.

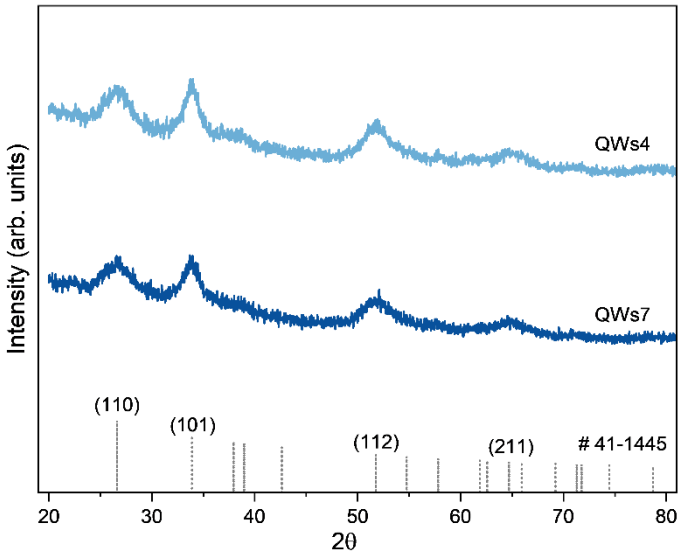

Supplementary Figure 2 | Comparison of XRD spectra of QWs4 and QWs7. After complete removal of surface capping ligands, the X-ray diffraction (XRD) patterns of the synthesized sub-nanometer SnO_2 quantum wires exhibit broad reflections that match well with the standard tetragonal phase of SnO_2 ($P4_2/mnm$, JCPDS No. 41-1445), confirming the formation of phase-pure crystalline QWs. The pronounced broadening of the diffraction peaks indicates reduced coherent scattering domains, consistent with their ultrasmall particle size and high density of surface defects, which collectively contribute to elevated surface energy.

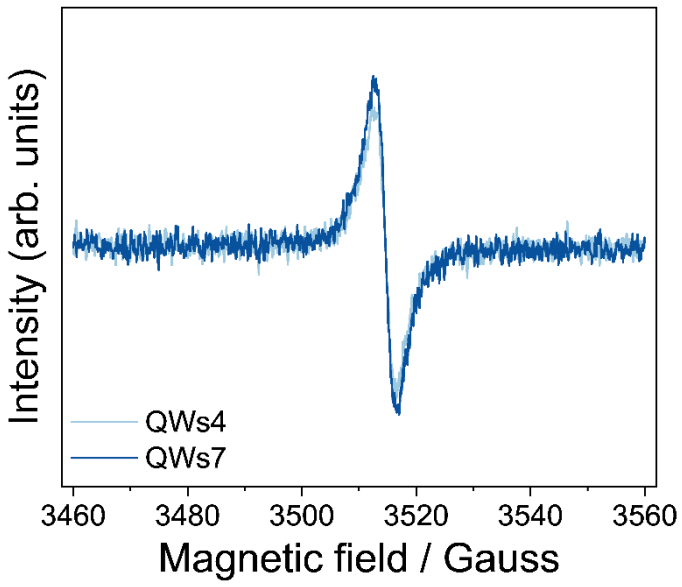

Supplementary Figure 3 | Comparison of the EPR spectra of QWs4 and QWs7. All QW samples exhibited a sharp resonance signal at g = 2.002, attributed to surface-adsorbed superoxide species (O_2^-) generated via interaction of atmospheric oxygen with under-coordinated lattice oxygen sites — consistent with prior reports on defect-rich oxide surfaces[1]. The signal intensity progressively increased with prolonged solvothermal treatment, indicating a time-dependent accumulation of singly ionized O_v centers. Quantitative analysis (Supplementary Table 1) of the EPR signal intensity revealed that the concentration of single-electron oxygen vacancies increased from 9.16 × 10^{12} spins g^{-1} (QWs4) to 1.09 × 10^{13} spins g^{-1} (QWs7). The increase follows a saturation-like behavior, suggesting a limit to vacancy formation under the given synthetic conditions.

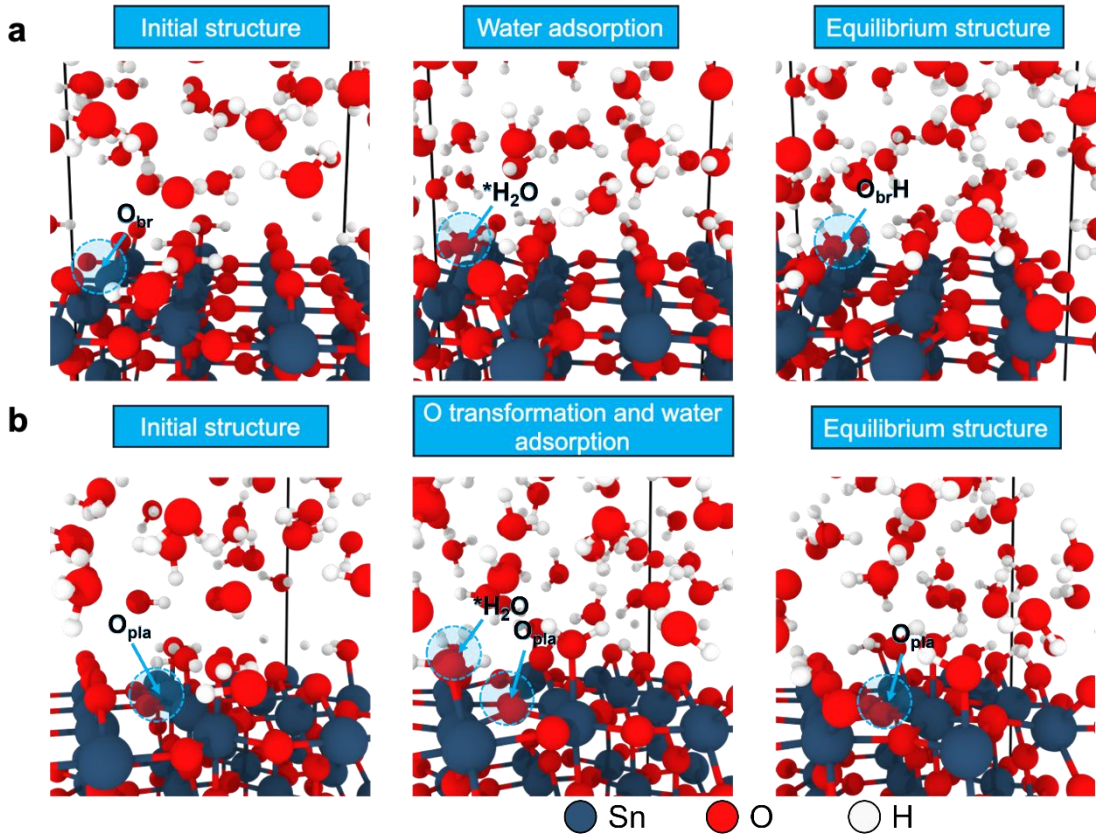

Supplementary Figure 4 | Surface vacancy transformation during molecular dynamics simulations. (a) Direct healing of a bridge oxygen vacancy (O_v). MLMD snapshots illustrate that a vacancy at the bridge site is directly replenished by an oxygen atom from a coordinated interfacial water molecule. This process is followed by spontaneous water dissociation, resulting in the formation of a stable surface hydroxyl (-OH) group and the release of a proton. (b) Relay healing of a planar oxygen vacancy (O_{pla}). The transformation proceeds via a two-step mechanism: the planar vacancy is initially filled by a neighboring bridge oxygen atom through local lattice rearrangement, effectively migrating the vacancy to a bridge site; the newly generated bridge vacancy then undergoes the same water-mediated healing and dissociation process described in Pathway A. These simulations provide direct computational evidence that both types of surface vacancies serve as precursors for the formation of active surface hydroxyl motifs.

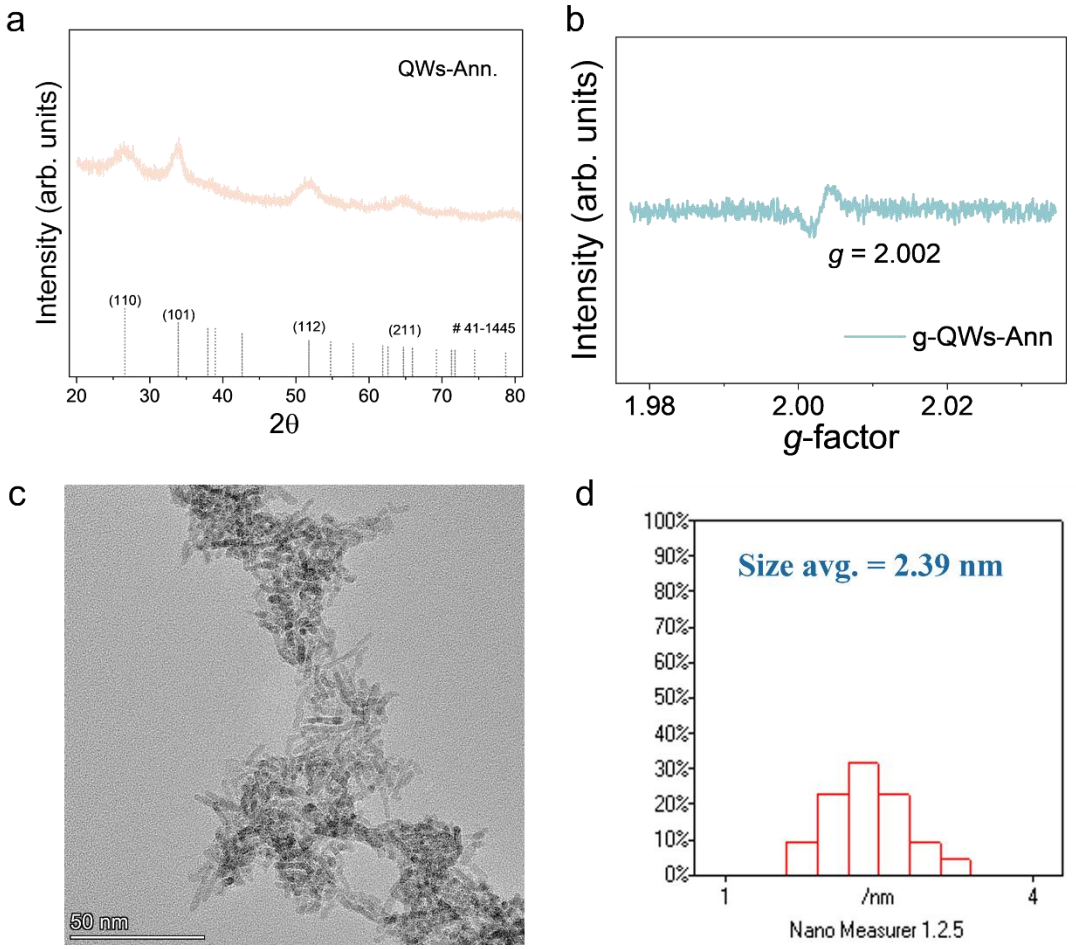

Supplementary Figure 5 | Crystal structure characterization of the air-annealed SnO_2 quantum wire samples (QWs-Ann). (a) X-ray diffraction (XRD) patterns, (b) EPR spectra, (c) high-resolution transmission electron microscopy (HRTEM) images, and (d) the particle size distribution histogram reveal that air-annealed QWs maintain the tetragonal rutile SnO_2 phase, consistent with JCPDS No. 41-1445, with no evidence of secondary phases. Despite defect healing, no significant changes in lattice symmetry or long-range crystallinity were observed, indicating that annealing primarily reduces surface oxygen vacancies without altering the bulk structure.

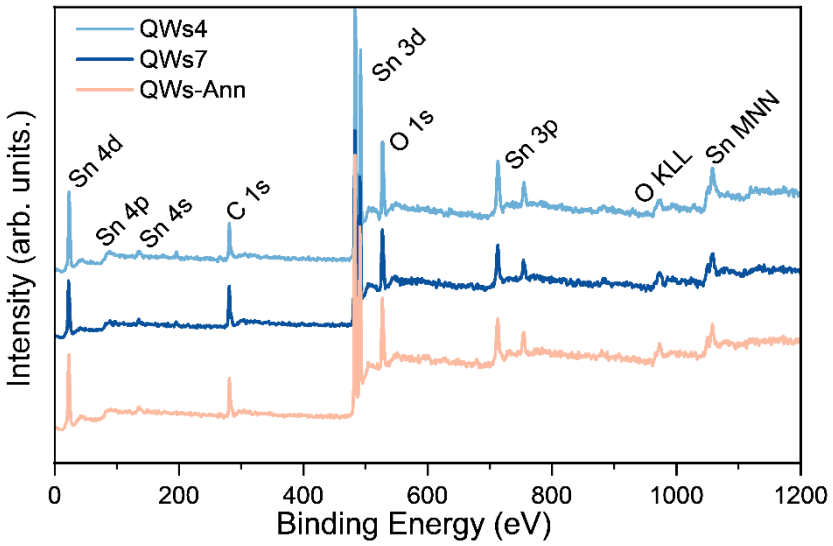

Supplementary Figure 6 | XPS survey spectra of the sample surfaces. The spectra have been linearly shifted to facilitate comparison.

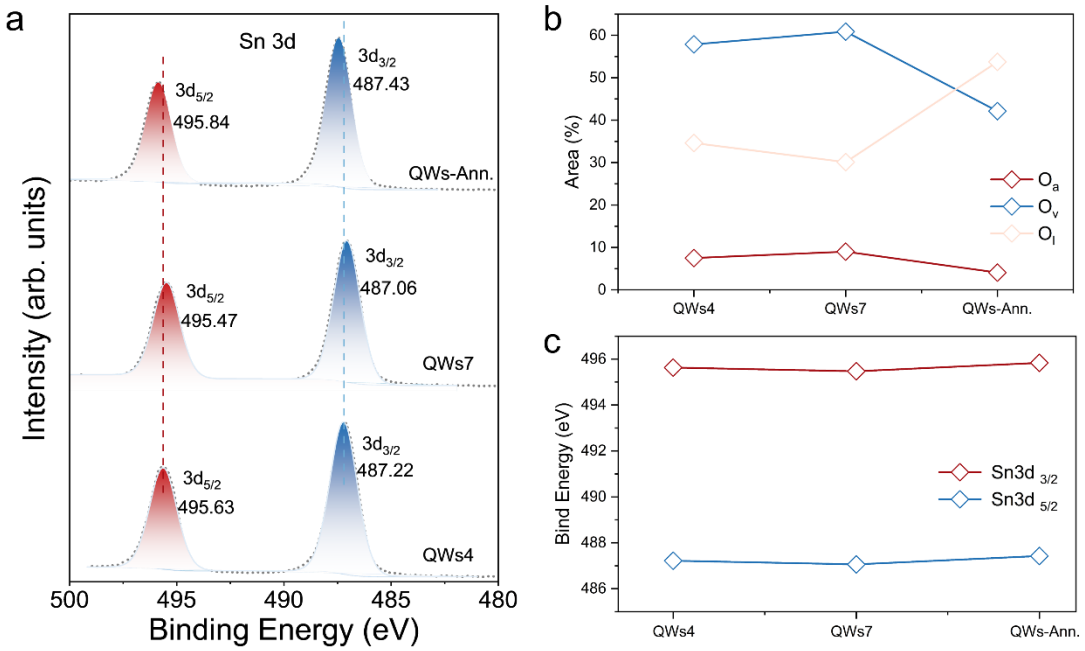

Supplementary Figure 7 | XPS analysis of surface oxygen and tin species. (a) High-resolution Sn 3*d* XPS spectra for QWs4, QWs7, and air-annealed QWs-Ann samples. (b) Relative proportions of O_a, O_v, and O_l derived from peak deconvolution of O 1*s* spectra. (c) Binding energy values of Sn $3d_{5/2}$ and Sn $3d_{3/2}$ peaks across samples, highlighting the redox evolution of surface Sn states with increasing oxygen vacancy concentration and subsequent reoxidation upon annealing.

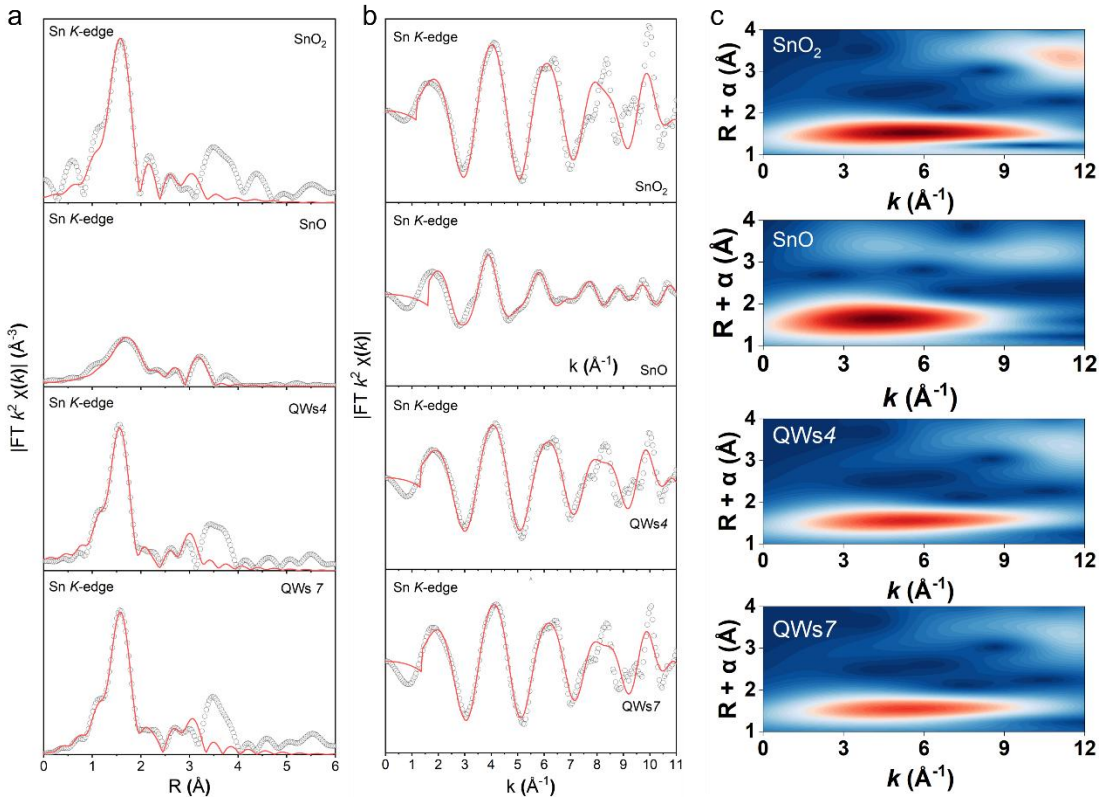

Supplementary Figure 8 | Local structural analysis of SnO_2 quantum wires (QWs) by Sn K-edge EXAFS. (a) Fourier-transformed (FT) magnitude of k^2-weighted EXAFS spectra, (|χ(R)|), for SnO_2, SnO, QWs4, and QWs7, showing first-shell Sn–O and second-shell Sn–Sn coordination. Here, R denotes the radial-distance coordinate in the phase-uncorrected FT-EXAFS spectra. (b) Corresponding k-space EXAFS oscillations, χ(k), and fitting curves, showing the agreement between experimental data (black dots) and fitted models (red lines). (c) Wavelet transform (WT) contour plots of the EXAFS data, revealing differences in backscattering contributions from O and Sn atoms. The QW samples exhibit diminished Sn–Sn scattering intensity, indicating increased structural disorder and reduced long-range coordination compared to bulk references. Coordination number (CN), Debye–Waller factor (σ^2), energy shift (E_0), and fitting residual factor (R-factor) are defined in the corresponding EXAFS fitting table. The diminished Sn–Sn scattering feature at an apparent radial distance of approximately 3.1–3.4 Å in the phase-uncorrected spectra is consistent with disrupted long-range order in the QW samples.

The EXAFS spectra of QWs4 and QWs7 reveal a systematically reduced Sn–O coordination number (CN ≈ 5.2 and 5.1, respectively) compared to bulk SnO_2 (CN ≈ 6.1), suggesting a significant concentration of under-coordinated Sn sites arising from oxygen vacancies. The first-shell Sn–O bond lengths remain consistent at ~2.05–2.06 Å across all samples, indicating the preservation of local bonding geometry despite vacancy-induced disruption. The Debye–Waller factors (σ^2) associated with the Sn–O shell in QWs4 and QWs7 remain low (≤ 0.003 $Å^2$), implying minimal static disorder, while the slightly elevated σ^2 in SnO confirms greater structural heterogeneity. The

second-shell Sn–Sn scattering path shows a marked attenuation in QWs4 and QWs7, with CN values of ~2.0-2.1 compared to 2.3 in SnO_2 and SnO, indicating disrupted long-range order. This is further corroborated by the WT maps, where the characteristic Sn–Sn scattering feature (~3.1-3.4 Å in R + α) is visibly diminished in QW samples. These observations collectively confirm the nanoscale nature and defect-rich structure of the QW catalysts. Notably, the E_0 shift values are positively correlated with increased vacancy concentration, with QWs4 and QWs7 exhibiting higher shifts (~6.5–7.3 eV), consistent with the increased electron density at Sn centers due to vacancy-induced local reduction. The low R-factors (≤ 0.02) across all fittings validate the robustness and reliability of the EXAFS models. Taken together, these results affirm that the QW samples possess abundant undercoordinated Sn sites and bridging oxygen vacancies, which are critical for generating bidentate hydroxyl species ($-O_{br}H$) and enhancing water dissociation activity.

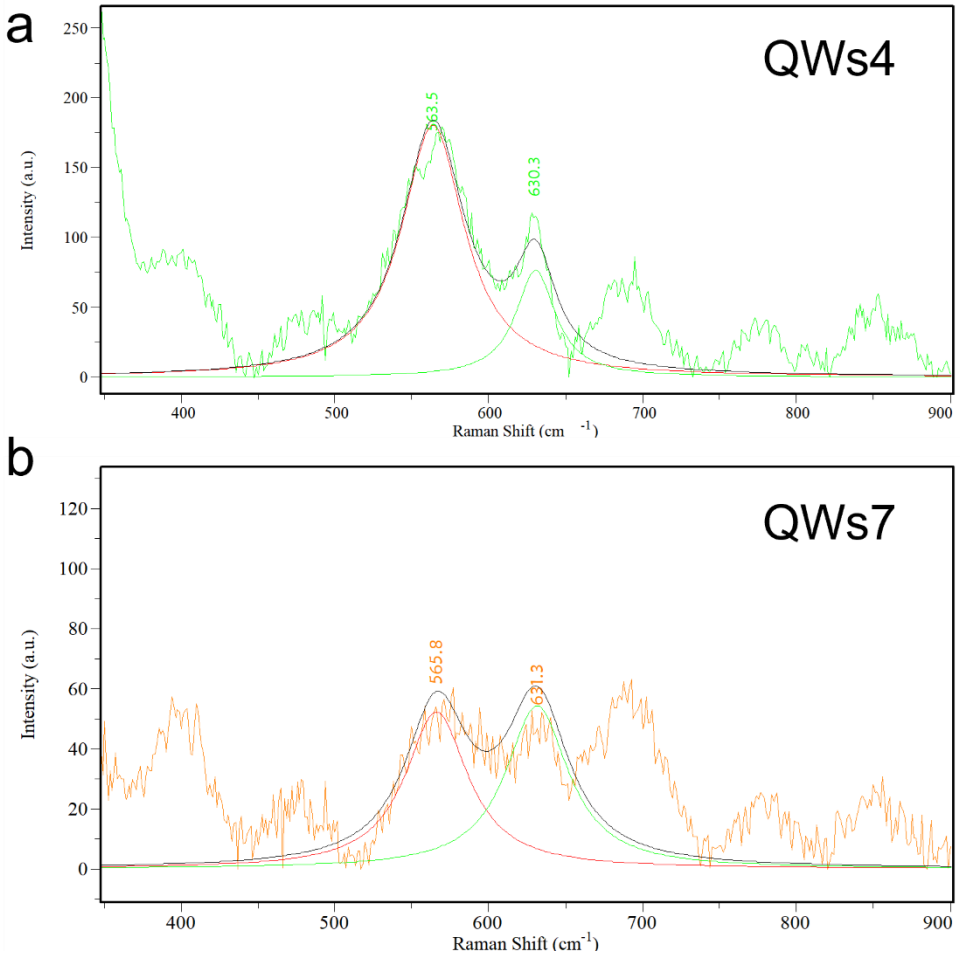

Supplementary Figure 9 | Fitting analysis of Raman spectra for (a) QWs4, and (b) QWs7. The spectra were deconvoluted using Gaussian fitting algorithms in LabSpec5 (HORIBA Scientific). Raw data were used without pre-processing. The two major Raman bands corresponding to in-plane (i-O_vs, ~563–569 cm^{-1}) and bridging oxygen vacancies (b-O_vs, ~630–633 cm^{-1}) were fitted, and the resulting peak areas are summarized in Supplementary Table 4 for quantitative comparison. The fitting was performed using Gaussian mixed profiles with baseline correction. The increasing b-O_v/i-Ov ratio from QWs4 to QWs7 reflects a progressive enrichment of bridging oxygen vacancies with increasing solvothermal duration. Intensity is plotted in arbitrary units (a.u.), as exported directly from the Raman fitting software.

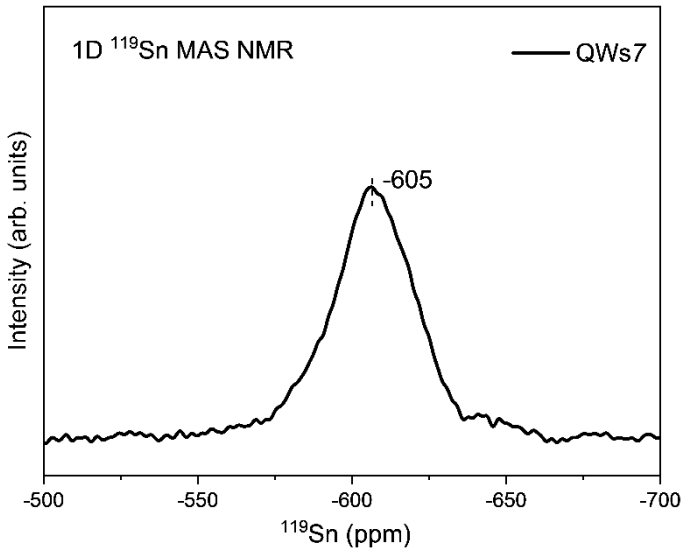

Supplementary Figure 10 | ^{119}Sn MAS NMR spectra of QWs7, acquired at a magic angle spinning (MAS) rate of 10 kHz. The spectral acquisition was performed under a static magnetic field strength of 9.4 T, with a sampling rate (SR) of 127.965 kHz.

The main resonance centered around 605 ppm is characteristic of SnO_6 octahedra in the tetragonal SnO_2 structure. The broadened and partially split lineshape indicates the presence of multiple structural configurations of SnO_2 units, reflecting a wide distribution of bond angles and bond lengths.

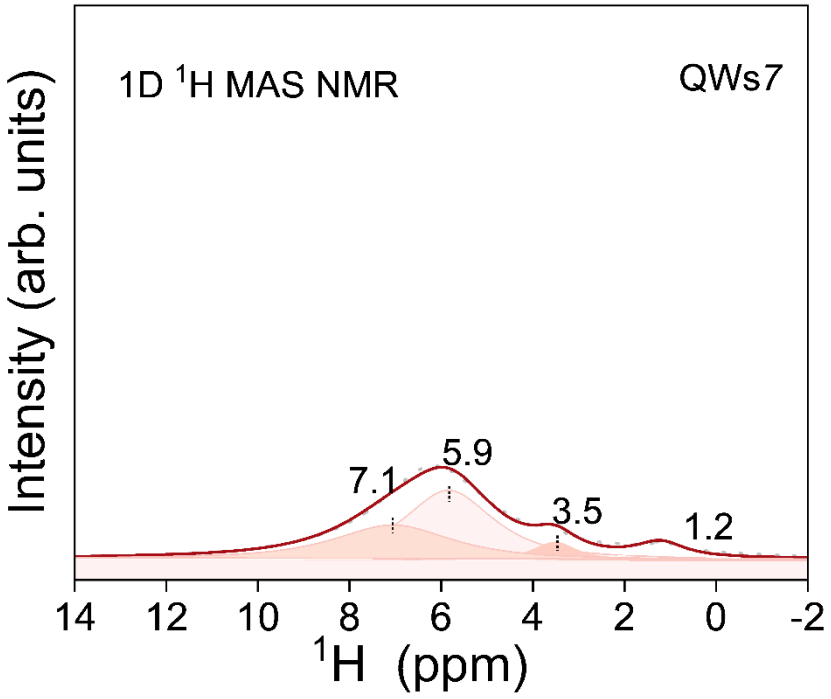

Supplementary Figure 11 | ^{1}H MAS NMR spectra of QWs7, acquired at a magic angle spinning (MAS) rate of 10 kHz. The spectral acquisition was performed under a static magnetic field strength of 9.4 T, with a sampling rate (SR) of 127.965 kHz.

Deconvolution of the ^{1}H NMR spectrum of the QWs7 sample reveals four resonance peaks at 7.1, 5.9, 3.5, and 1.2 ppm, with the peak at 1.2 ppm corresponding to isolated water molecules. In addition, hydroxyl groups bound to five- and six-coordinated tin on the surface of SnO_2 nanoparticles give rise to two distinct peaks, assigned to b-hydroxyl groups (7.1 ppm) and t-hydroxyl groups (5.9 ppm), respectively. The resonance peak at 3.5 ppm is close to the ^{1}H chemical shift in bulk water[2].

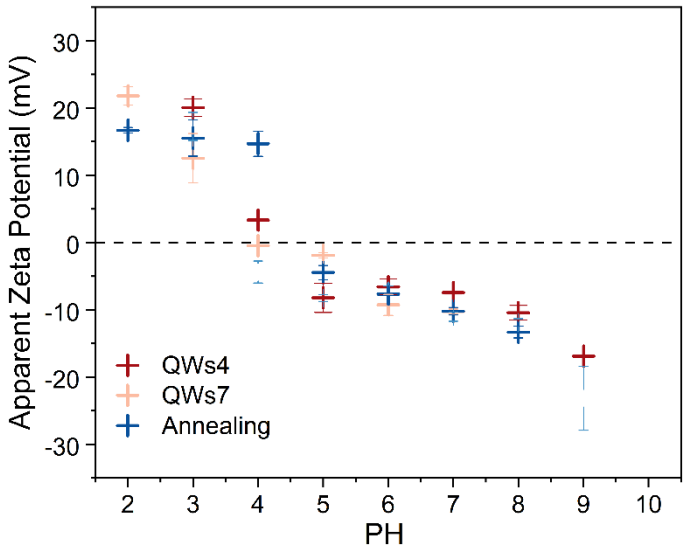

Supplementary Figure 12 | Determination of the point of zero charge via electrophoretic mobility measurements and dynamic light scattering. The SnO_2 QWs exhibit point of zero charge (PZC) values ranging from pH 3 to pH 12, with an experimental uncertainty of ±0.5 pH units. To ensure measurement accuracy, each catalyst was tested in five independent replicates. The average value is reported in the manuscript, and the standard deviation is rounded to the nearest 0.5 pH unit to represent the error. Detailed procedures are provided in the Methods section.

The acid–base behavior of metal hydroxides depends on the degree of polarization of adsorbed water molecules or hydroxide ions. This consideration similarly applies to hydroxyl groups coordinated to metal oxide surfaces. At a specific pH where the net surface charge becomes neutral, the oxide is said to reach its "zero point of charge" (ZPC), which typically corresponds closely to that of the metal hydroxide. In SnO_2 QWs, the acid–base disparity among surface hydroxyls is governed by the nature of the oxygen vacancies, which directly impacts the interfacial charge behavior. The similarity in PZC values indicates the presence of partial water dissociation at this proton-hopping interface, which is consistent with the acid–base equilibrium characteristics of the SnO_2 surface[3,4].

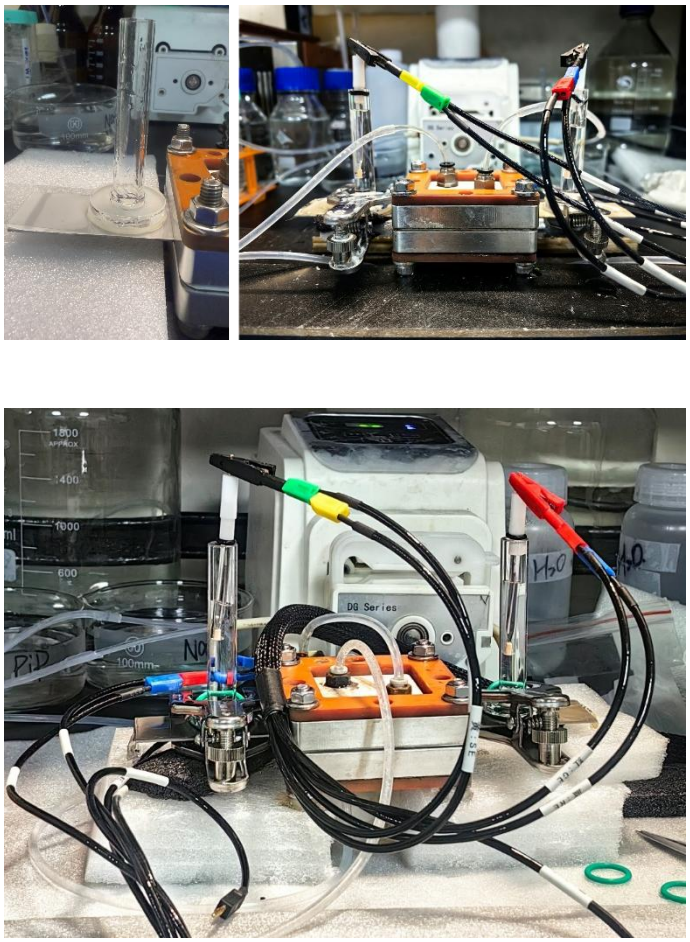

Supplementary Figure 13 | Assembly and operation of the BPM electrolyzer used for TMV detection. Photographs of the membrane-sensing setup. Anion-exchange (AEL) and cation-exchange (CEL) membrane strips are connected to the corresponding BPM layers, each with a reference electrode. A dual-channel potentiostat is used to apply current and measure the transmembrane voltage.

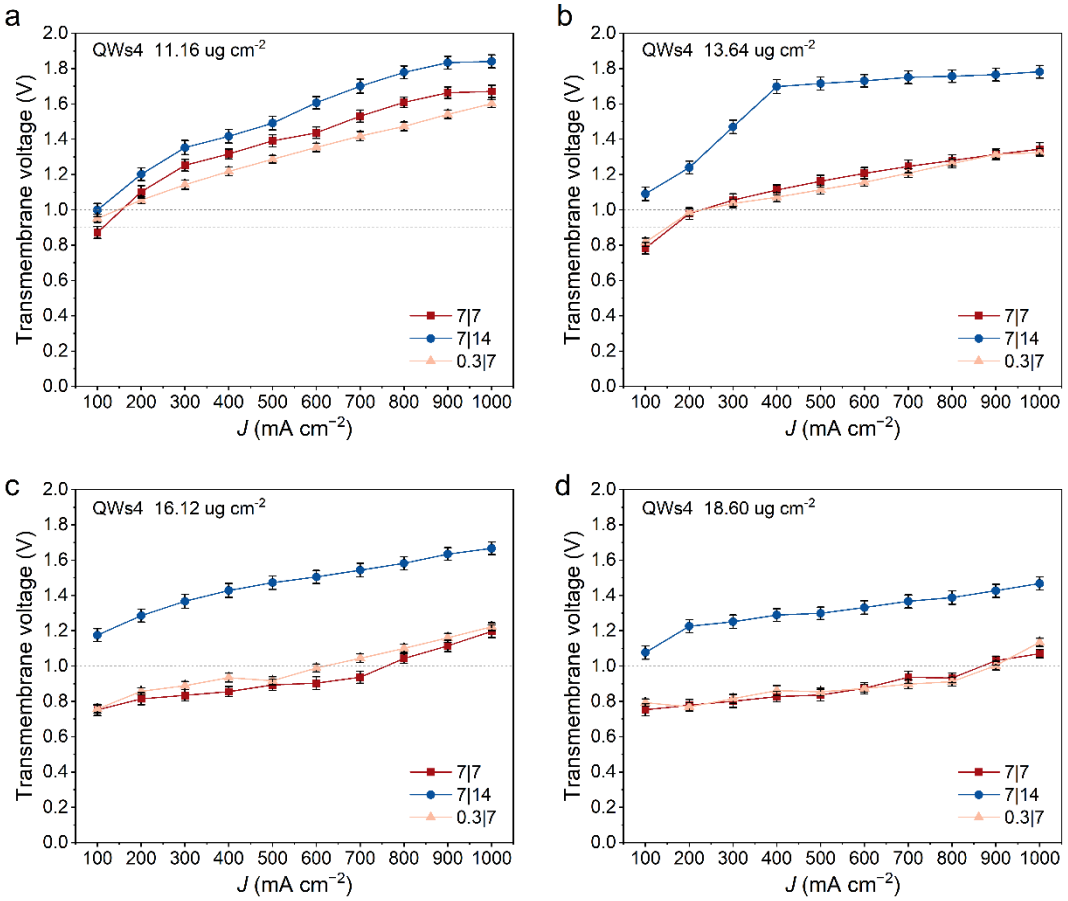

Supplementary Figure 14 | TMVs at different current densities for BPM electrolyzers employing QWs4 as the water dissociation (WD) catalyst at varying loadings: (a) 11.16, (b) 13.64, (c) 16.12, and (d) 18.60 μg cm^{-2}, under three distinct pH conditions: (7|7), (7|14), and (0.3|7).

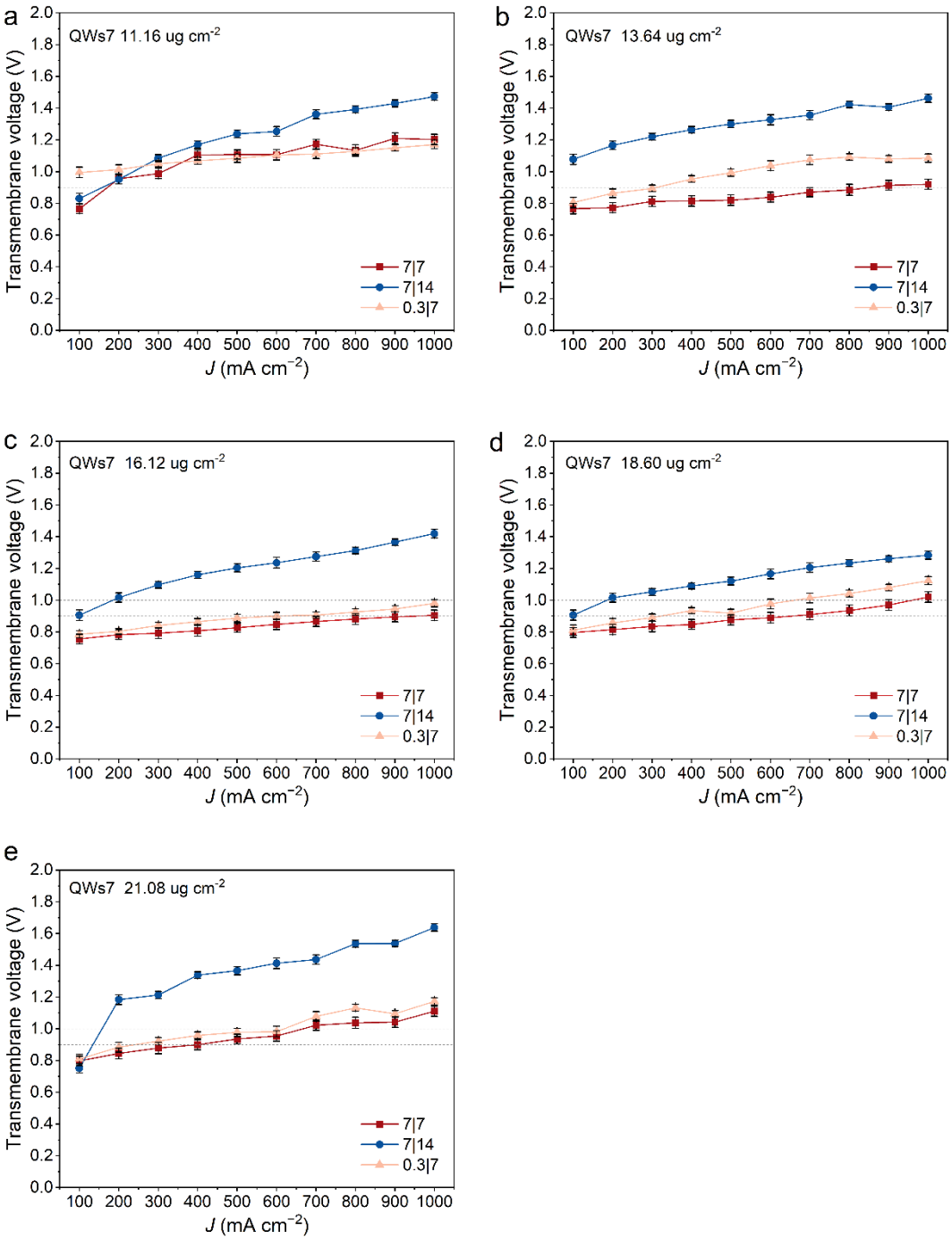

Supplementary Figure 15 | TMVs at different current densities for BPM electrolyzers employing QWs7 as the water dissociation (WD) catalyst at varying loadings: (a) 11.16, (b) 13.64, (c) 16.12, (d) 18.60, and (e) 21.08 μg cm^{-2}, under three distinct pH conditions: (7|7), (7|14), and (0.3|7).

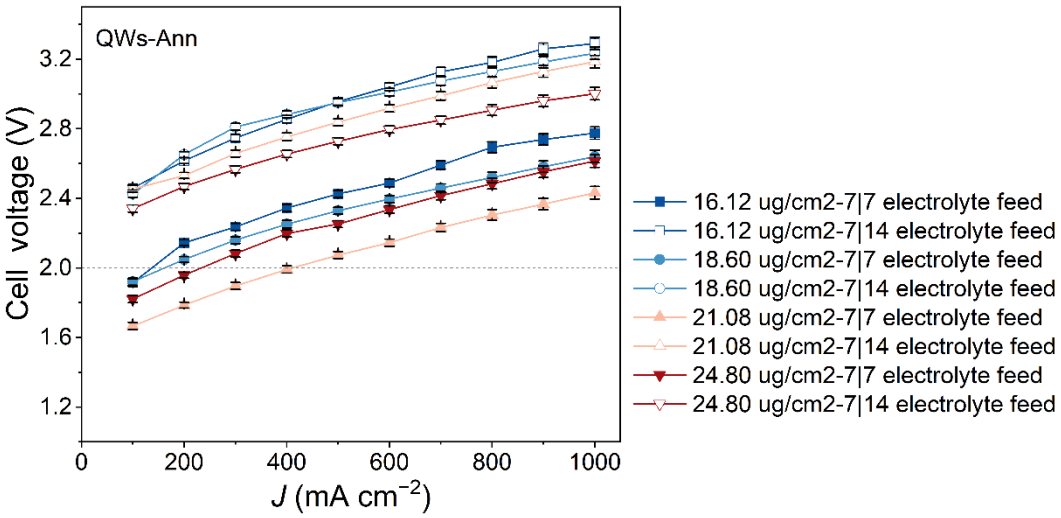

Supplementary Figure 16 | Full cell polarization curves of BPM electrolyzers employing QWs-Ann. as the water dissociation (WD) catalyst at varying loadings: 16.12, 18.60, 21.08, and 24.08 μg cm^{-2}, under two distinct pH gradient conditions: (7|7) and (7|14).

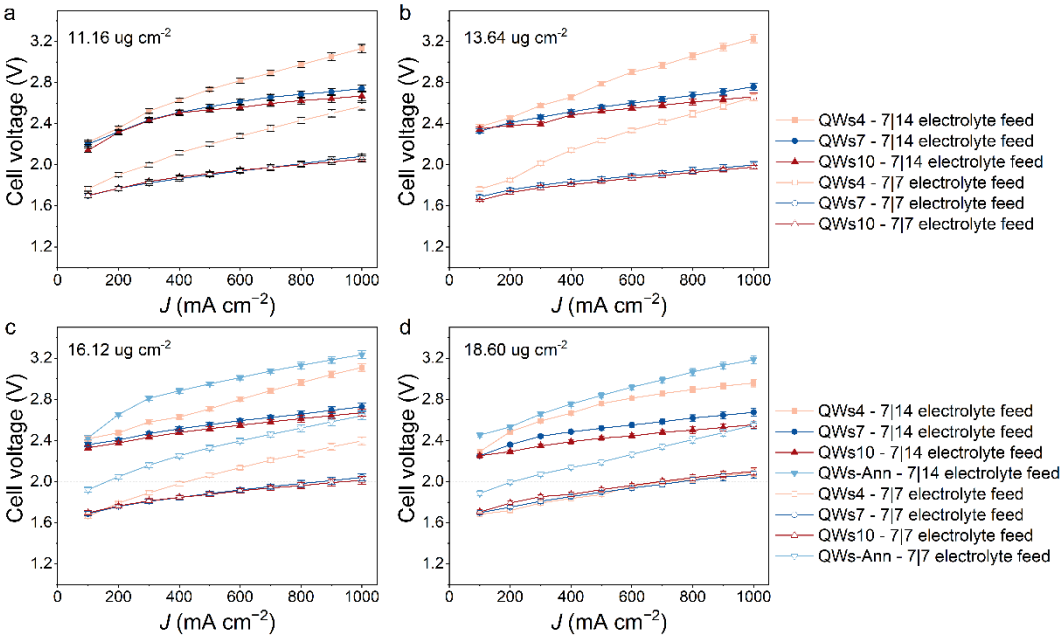

Supplementary Figure 17 | Full-cell polarization curves of BPM electrolyzers employing SnO_2 QWs as the water dissociation (WD) catalyst at varying loadings: (a) 11.16, (b) 13.64, (c) 16.12, and (d) 18.60 μg cm^{-2}, under two distinct pH gradient conditions: (7|7) and (7|14).

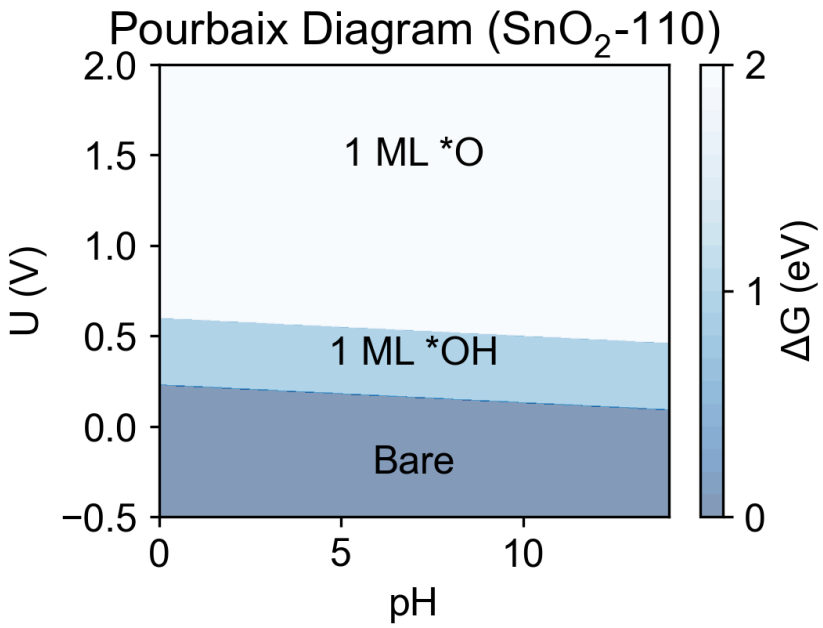

Supplementary Figure 18 | Surface Pourbaix diagram of SnO_2(110) with different terminations.

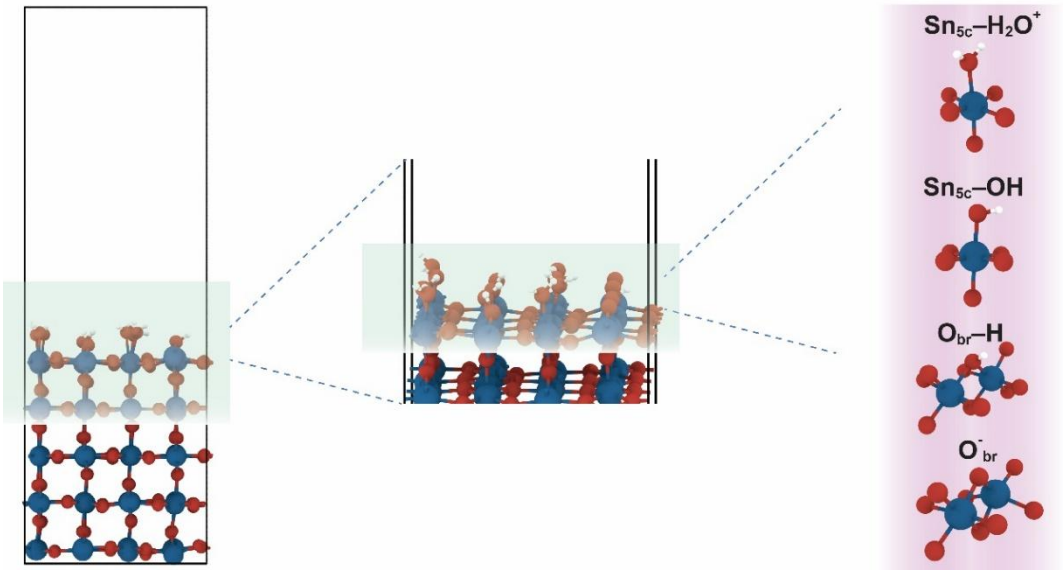

Supplementary Figure 19 | Representative equilibrium surface configurations obtained from MD simulations. An enlarged view of the SnO_2(110) surface is shown on the right, highlighting different types of adsorbed hydroxyl and water species, including Sn_{5c}−H_2O^+, Sn_{5c}−OH, −O_{br}H, and −O_{br}^-.

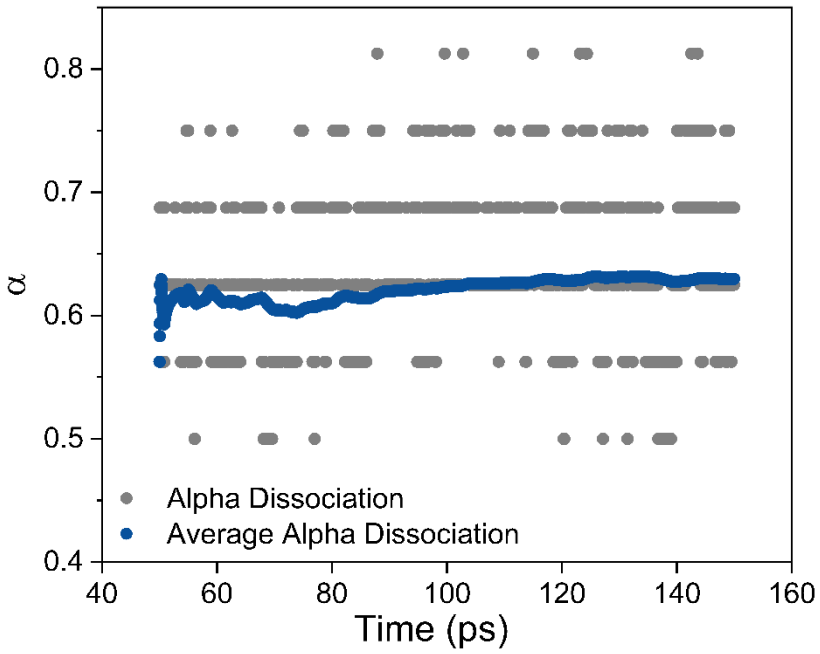

Supplementary Figure 20 | Time evolution of the structural parameter obtained from molecular dynamics simulations. Gray dots represent the instantaneous values, while the blue curve indicates the time-averaged trajectory. After a rapid relaxation within the first 10 ps, the value stabilizes at approximately 0.63, signifying that the system reaches a quasi-equilibrium state within the simulated timescale. The water dissociation value on the SnO_2 (110) surface, with the value (0.63) corresponding to the dissociation energy of -0.03 eV.

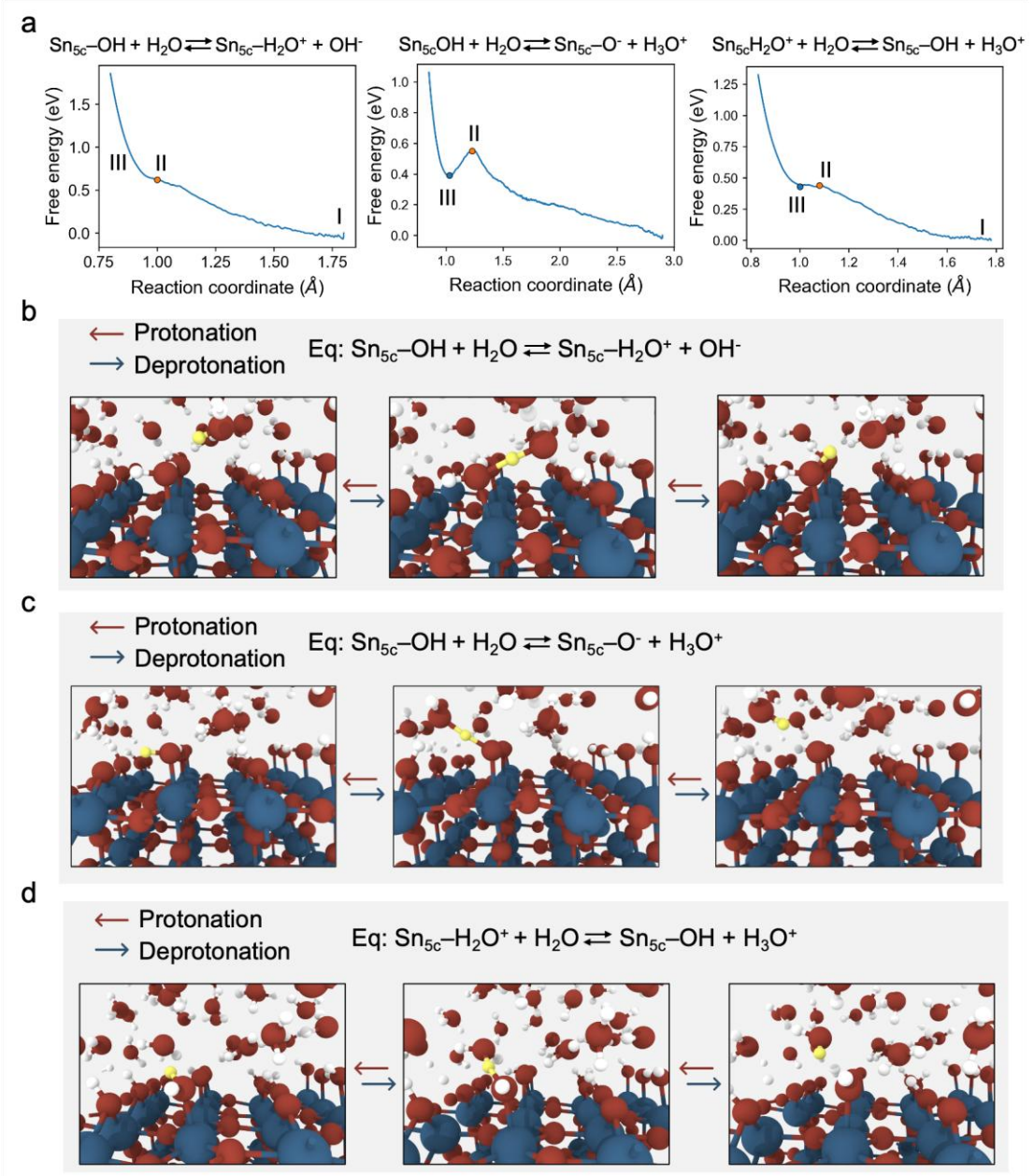

Supplementary Figure 21 | (a) Free energy profile at the Sn_{5c} site with different intermediates. (b) Snapshots of Sn_{5c}–OH being protonated by water to form Sn_{5c}–H_2O^+. (c) Snapshots of Sn_{5c}–OH being deprotonated by water to form Sn_{5c}–O^-. (d) Snapshots of Sn_{5c}–H_2O^+ being deprotonated to generate Sn_{5c}–OH. These images correspond to indices I, II, and III in Supplementary Figure 21a.

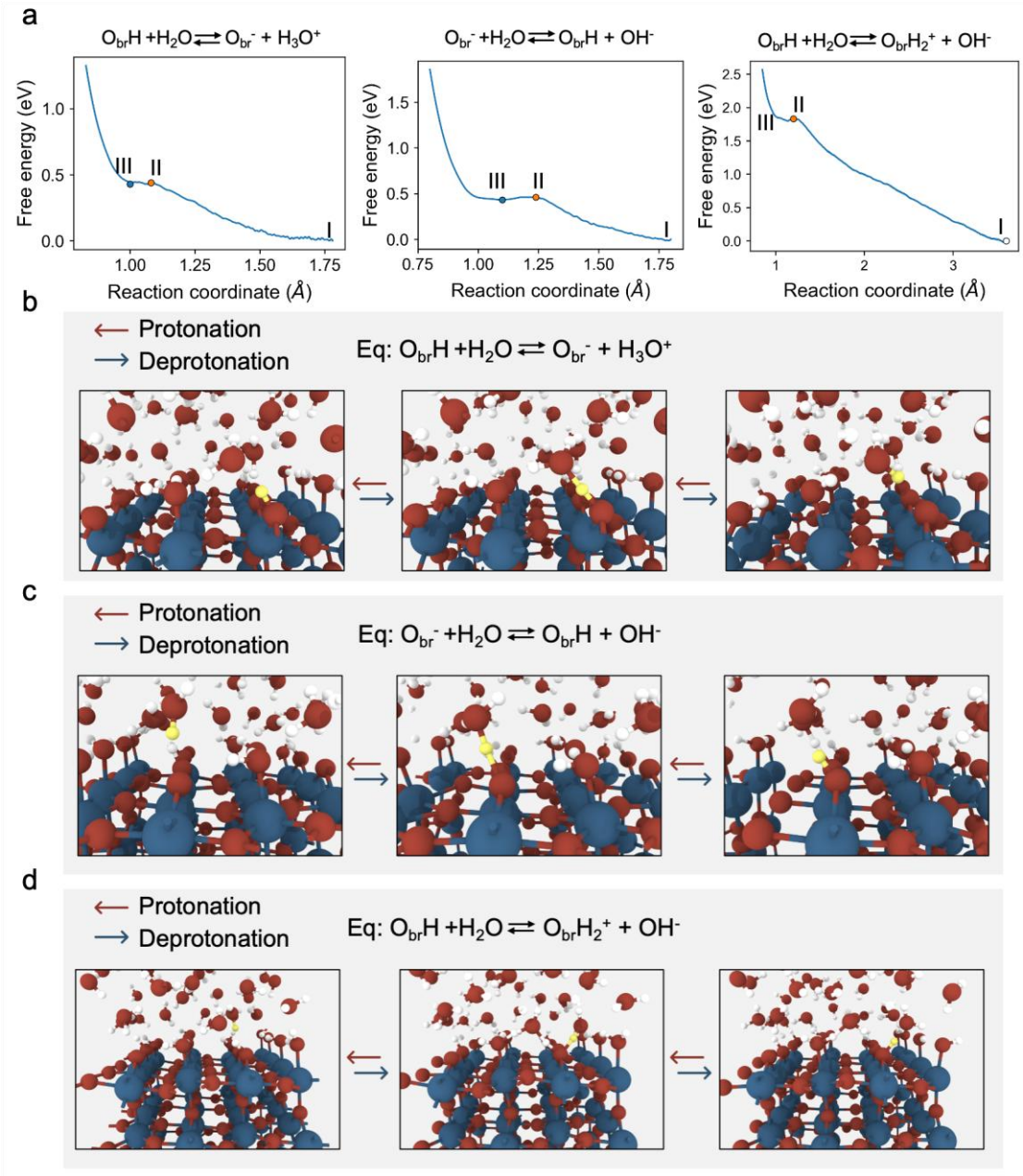

Supplementary Figure 22 | (a) Free energy profile at the $–O_{br}$ site with different intermediates. (b) Snapshot showing $–O_{br}H$ being deprotonated by water to form $–O_{br}^-$. (c) Snapshot showing $–O_{br}^-$ being protonated by water to form $–O_{br}H$. (d) Snapshot showing $–O_{br}H$ being protonated to generate $–O_{br}H_2^+$. These images correspond to indices I, II, and III in Supplementary Figure 22a.

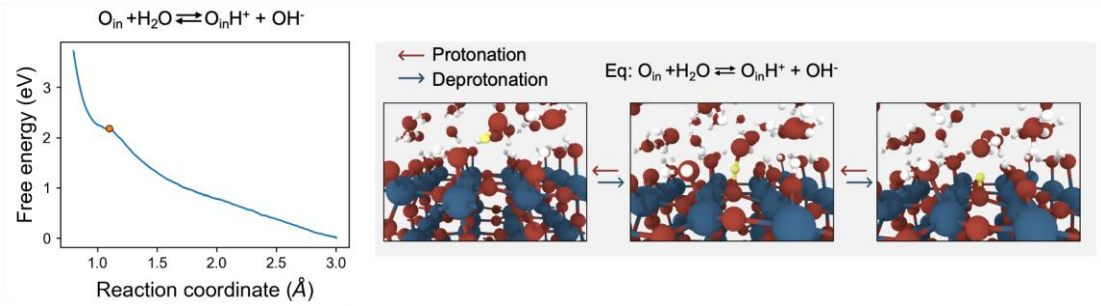

Supplementary Figure 23 | The protonation free energy profile on the O_{in} site, and the corresponding protonation trajectory.

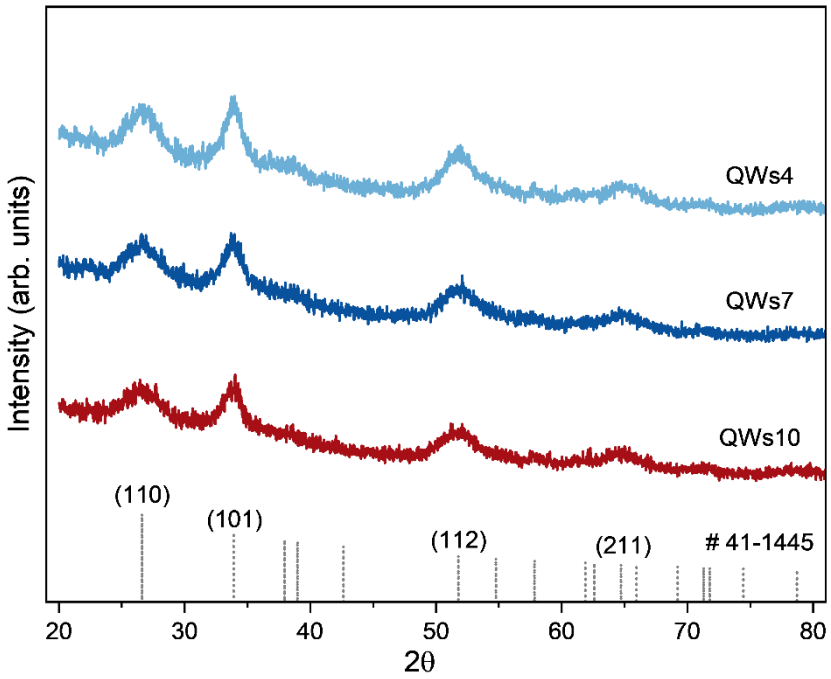

Supplementary Figure 24 | Comparison of XRD patterns of QWs.

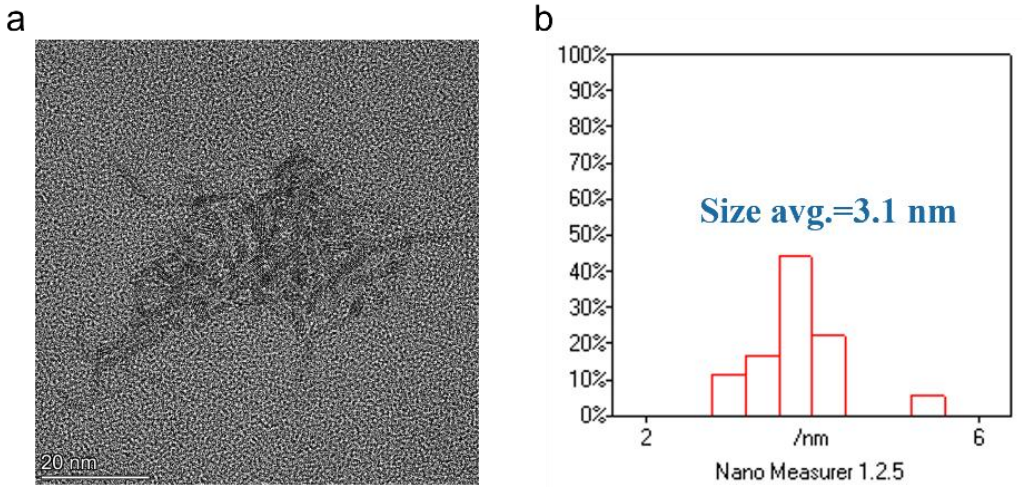

Supplementary Figure 25 | High-resolution transmission electron microscopy (HRTEM) images (a) and corresponding particle size distribution histograms (b) of QWs10.

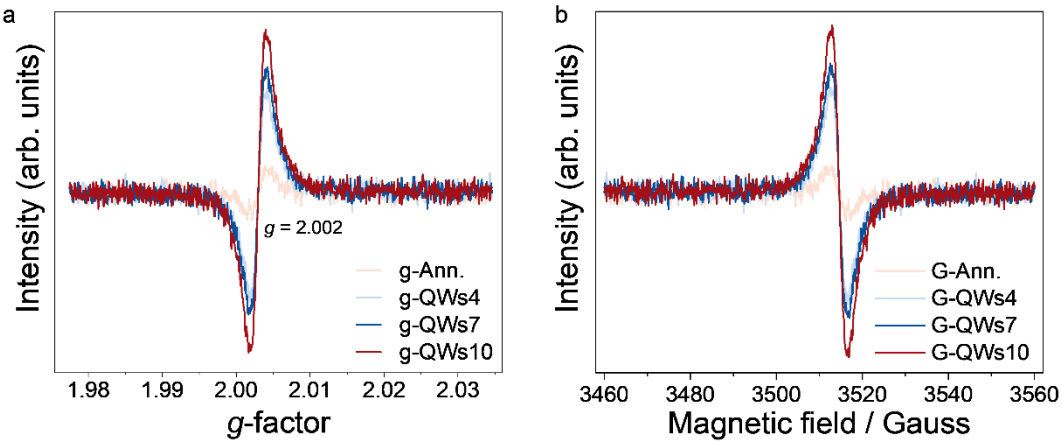

Supplementary Figure 26 | Comparison of EPR spectra of QWs-Ann, QWs4, QWs7, and QWs10. (a) EPR spectra plotted as a function of g-factor. (b) EPR spectra plotted as a function of magnetic field. The signal at g = 2.002 is assigned to superoxide species adsorbed at surface oxygen vacancies. Source data are provided as a Source Data file.

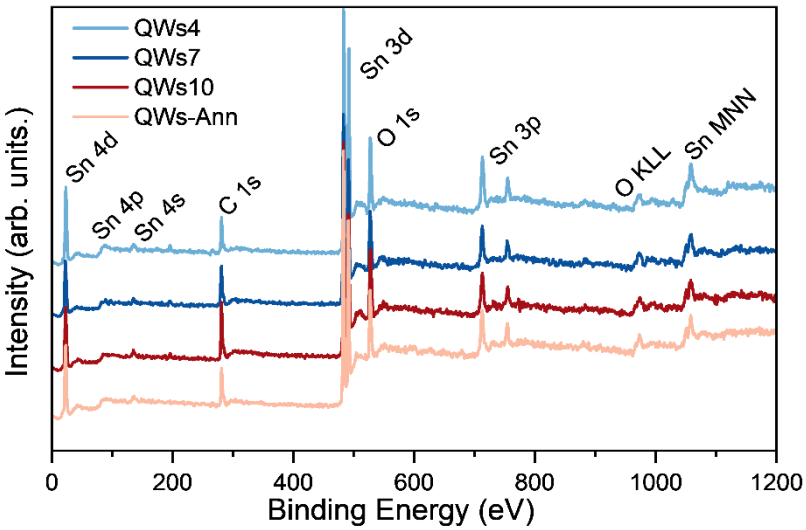

Supplementary Figure 27 | XPS survey spectra of different QWs catalysts.

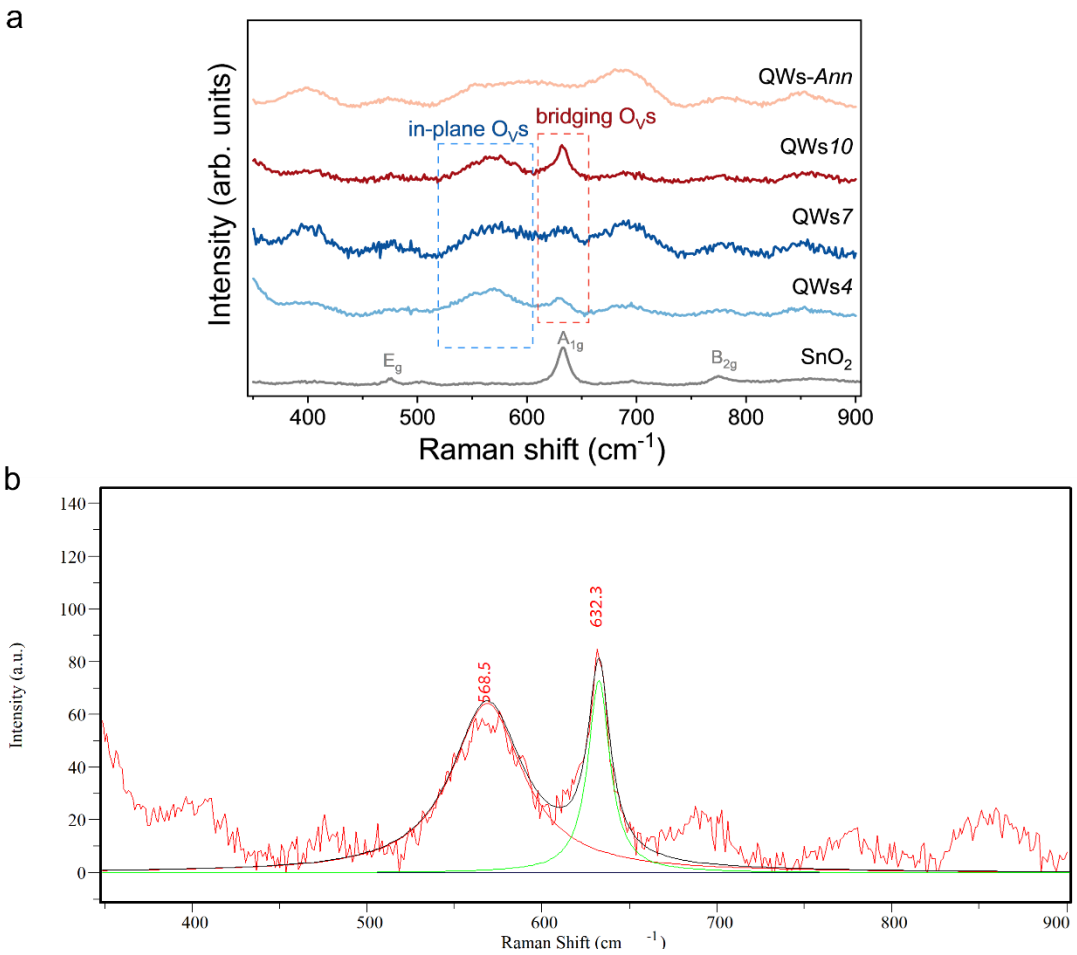

Supplementary Figure 28 | Raman analysis and peak deconvolution of QWs10. (a) Fitting analysis of Raman spectra of a series of QWs. (**b**) Gaussian peak deconvolution of the QWs10 Raman spectrum performed using LabSpec 5 (HORIBA Scientific). Raw data were used without pre-processing. Intensity is plotted in arbitrary units (a.u.), as exported directly from the Raman fitting software.

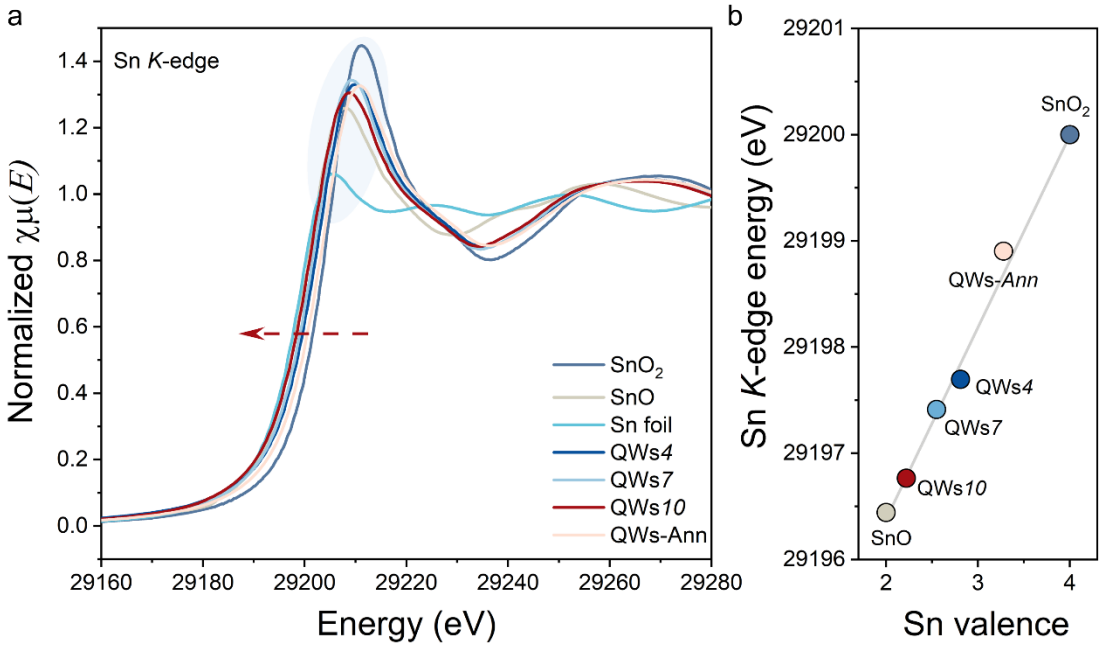

Supplementary Figure 29 | (a) Normalized Sn K-edge XANES spectra of QWs4, QWs7, QWs10, and QWs-Ann along with the Sn foil, SnO_2, and SnO references. (b) The average Sn oxidation states derived from K-edge XANES results.

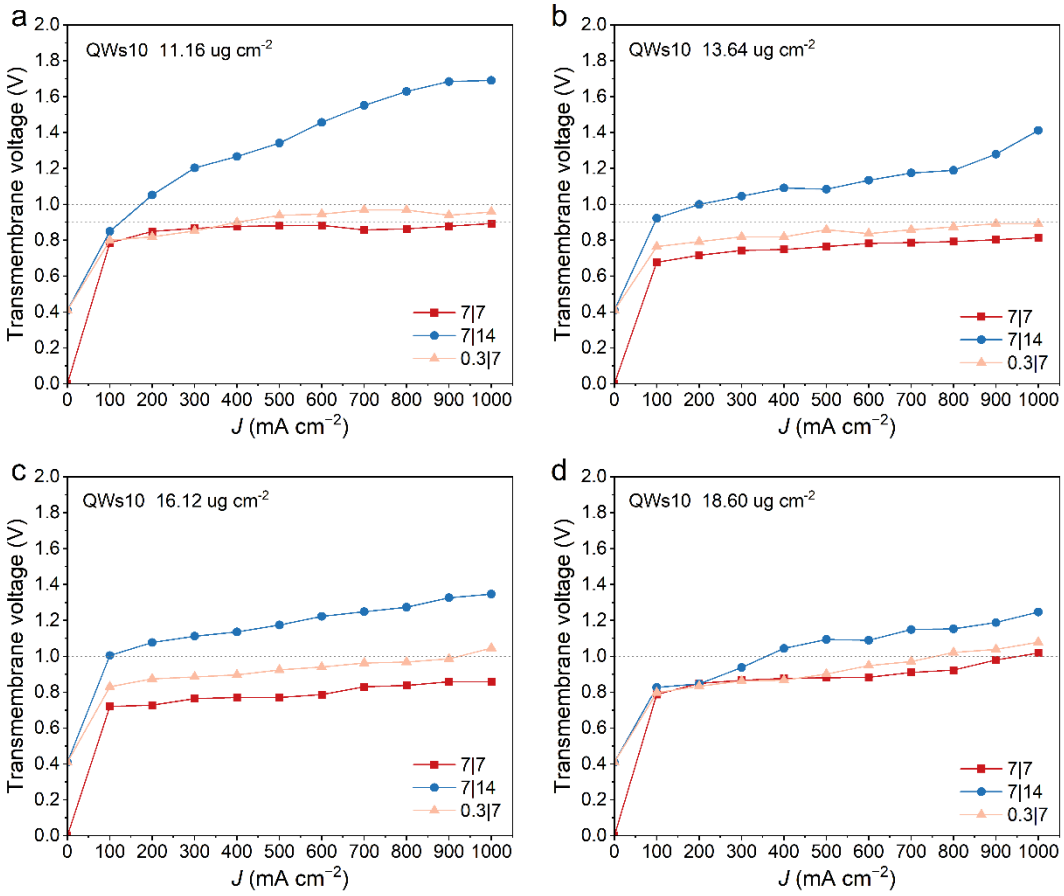

Supplementary Figure 30 | TMVs at different current densities for BPM electrolyzers employing QWs10 as the water dissociation (WD) catalyst at varying loadings: (a) 11.16, (b) 13.64, (c) 16.12, and (d) 18.60 μg cm^{-2}, under three distinct pH conditions: (7|7), (7|14), and (0.3|7).

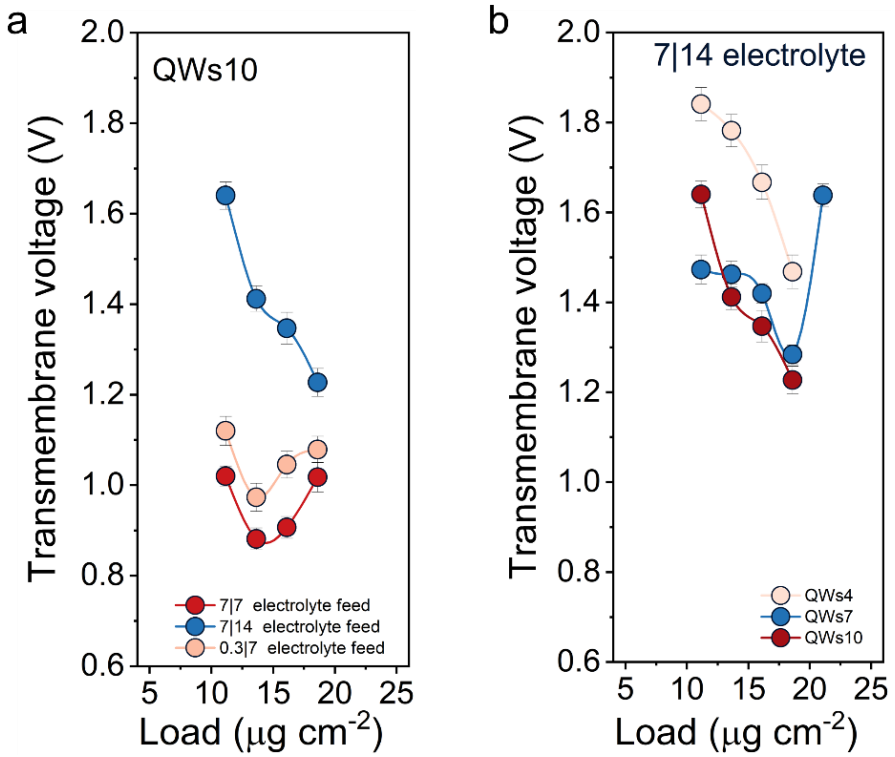

Supplementary Figure 31 | (a) TMVs at 1 A cm^{-2} for QWs7 presented as a function of catalyst loading under different electrolyte combinations. Measurements were conducted at room temperature (RT, 25 °C) without iR compensation. (b) TMVs at 1 A cm^{-2} for QWs4, QWs7, and QWs10 presented as a function of catalyst loading under the pH 7|14 electrolyte conditions.

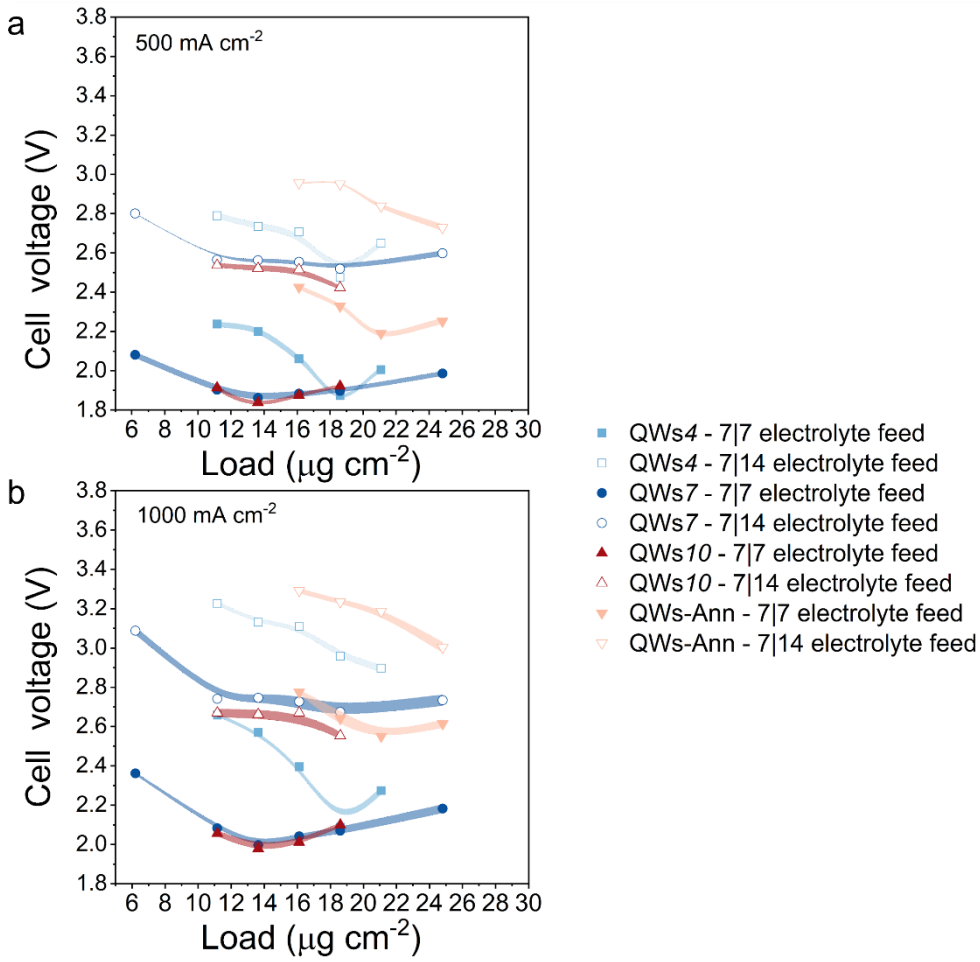

Supplementary Figure 32 | Cell voltages evaluated at (a) 500 and (b)1000 mA cm^{-2} for QWs presented as a function of catalyst loading.

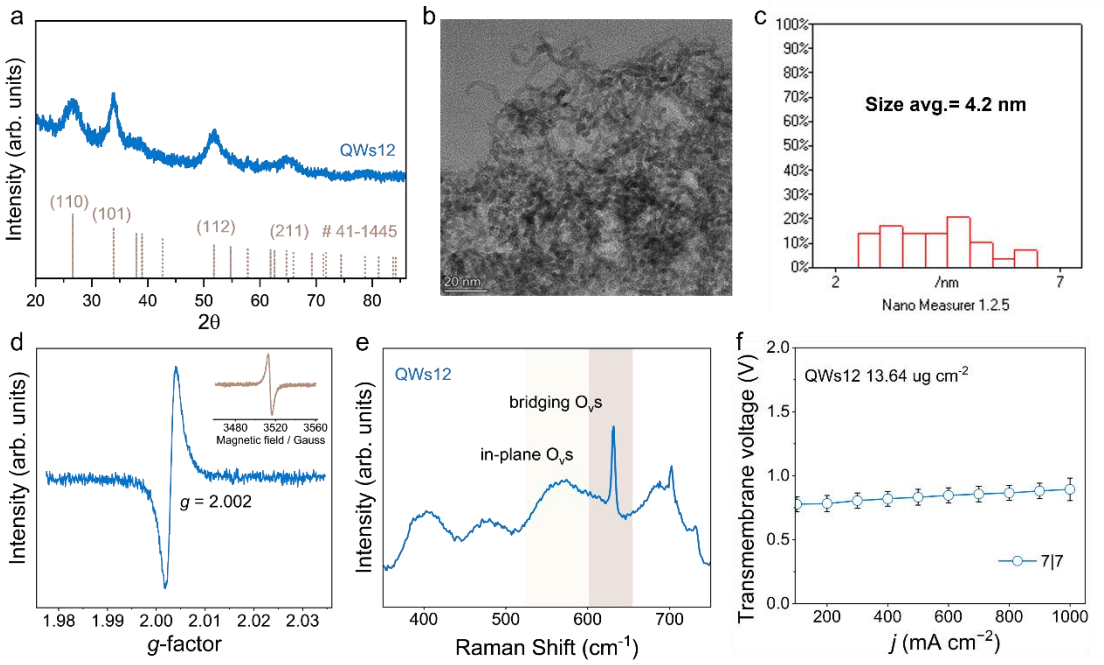

Supplementary Figure 33 | Characterization of SnO_2 QWs12. (a) PXRD patterns of QWs12. (b) High-resolution transmission electron microscopy (HRTEM) images and (c) corresponding particle size distribution histograms of QWs12. (d) EPR and (e) Raman spectra of QWs12. (f) TMV of a BPM electrolyzer employing QWs12 as the water dissociation (WD) catalyst at a loading of 14 μg cm^{-2} under pH 7|7 conditions.

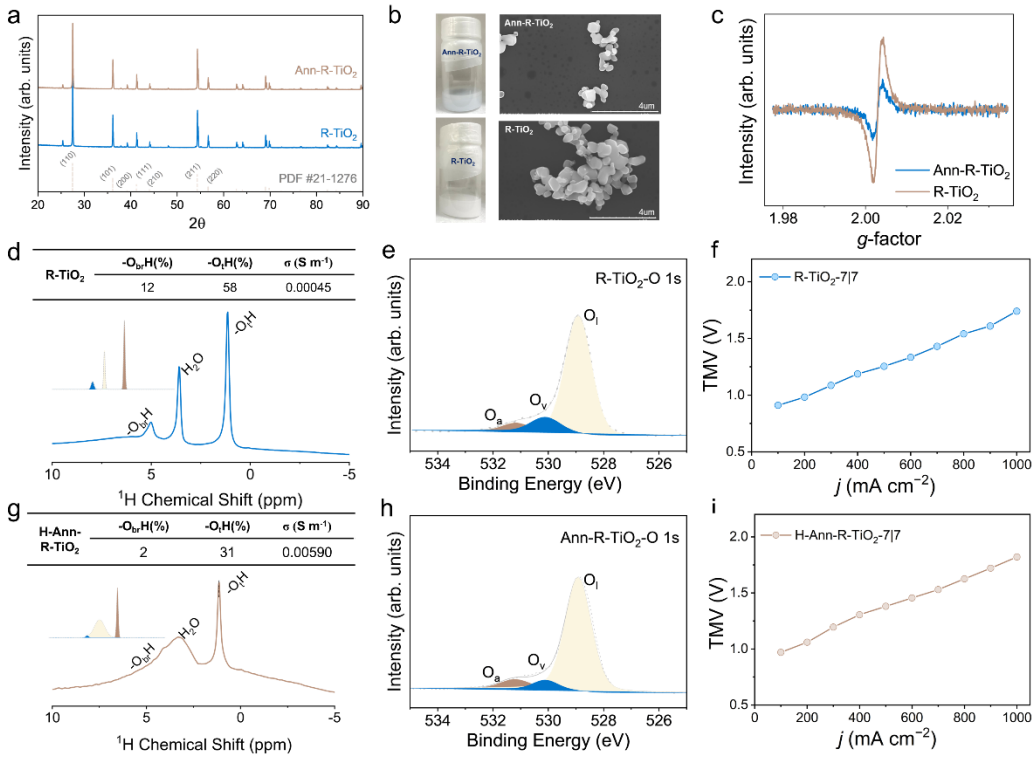

Supplementary Figure 34 | Characterization of R-TiO₂ and H-Ann-R-TiO₂. (a) PXRD patterns of pristine R-TiO_2 and hydrogen-treated H-Ann-R-TiO_2. All diffraction peaks are indexed to the rutile phase (PDF #21-1276), indicating that hydrogen treatment does not alter the bulk crystal structure. Inset: photographs of the corresponding catalyst inks. (b) Photographs and SEM images of R-TiO_2 and Ann- R-TiO_2. (c) Electron paramagnetic resonance (EPR) spectra indicating changes in paramagnetic defect species after H_2 treatment. Solid-state ^{1}H MAS NMR spectra and σ of (d) R-TiO_2 and (g) H-Ann-R-TiO_2. Resonances assigned to bridging hydroxyl, terminal hydroxyl, and adsorbed H_2O are indicated. O 1s XPS spectra of (e) R-TiO_2 and (h) H-Ann-R-TiO_2, deconvoluted into lattice oxygen (O_l), vacancy-associated oxygen (O_v), and surface hydroxyl/adsorbed oxygen species (O_a). TMV of BPM electrolyzers employing (f) R-TiO_2 and (i) H-Ann-R-TiO_2 as the water dissociation (WD) catalyst at a loading of 14 μg cm^{-2} under pH 7|7 conditions.

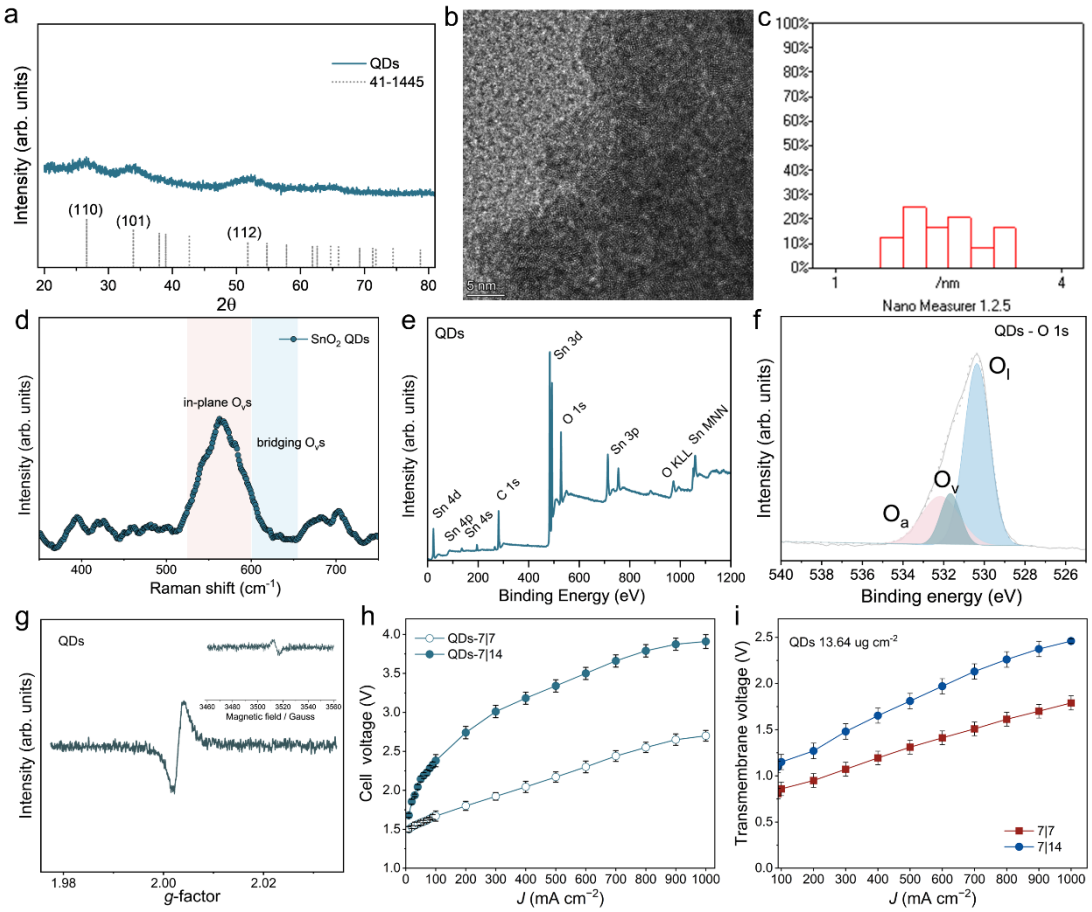

Supplementary Figure 35 | Characterization of SnO_2 QDs. (a) PXRD patterns of QDs. (b) High-resolution transmission electron microscopy (HRTEM) images and (c) corresponding particle size distribution histograms of QDs. (d) Raman, (e) XPS, and (g) EPR spectrum of QDs. (f) O 1s XPS spectra of QDs, deconvoluted into lattice oxygen (O_l), vacancy-associated oxygen (O_v), and surface hydroxyl/adsorbed oxygen species (O_a). (h) Full-cell polarization curve and (i) TMV of a BPM electrolyzer employing QDs as the water dissociation (WD) catalyst at a loading of 14 μg cm^{-2} under pH 7|7 and pH 7|14 conditions.

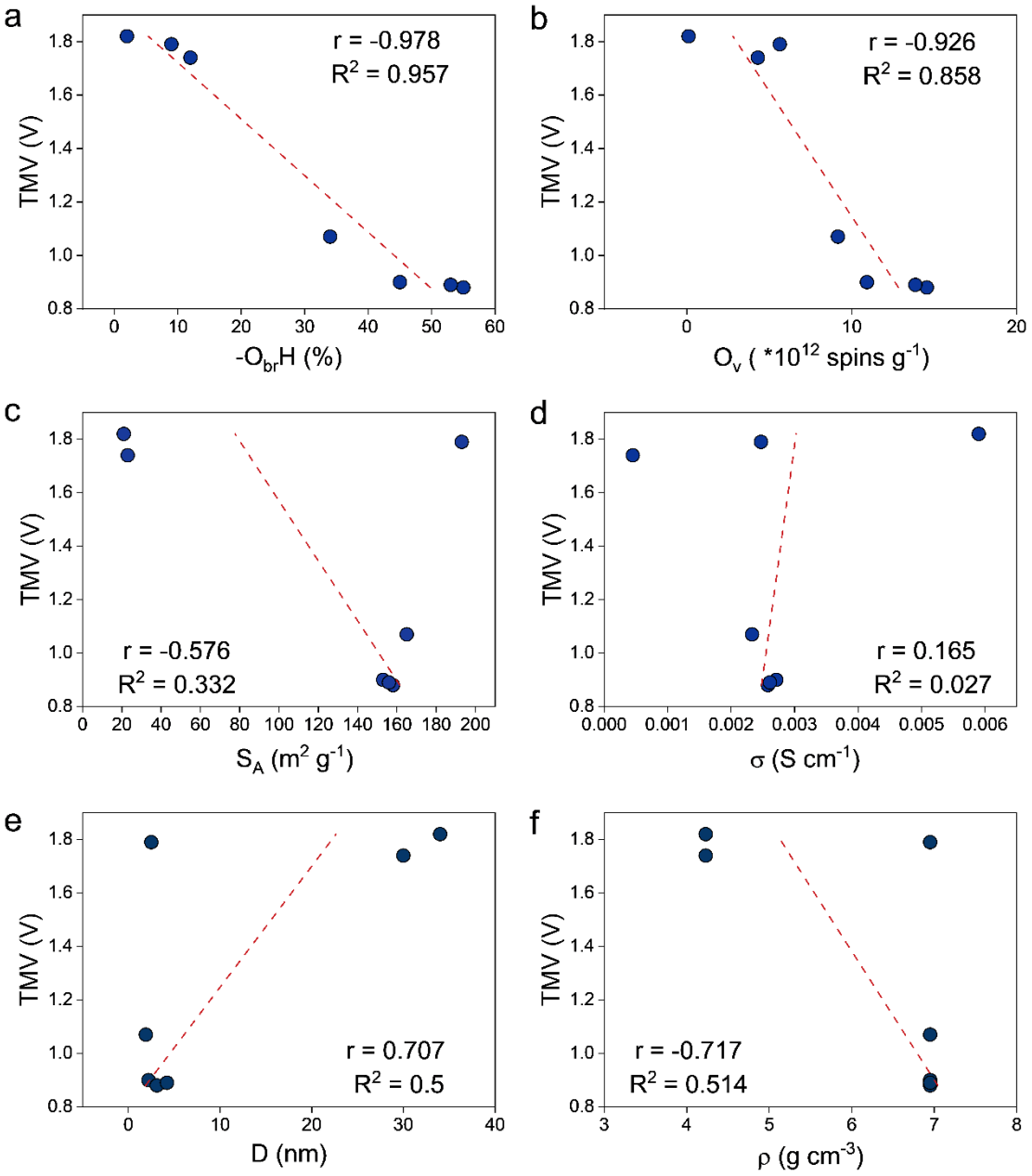

Supplementary Figure 36 | Correlation between TMV and individual physicochemical variables. Scatter plots showing the dependence of transmembrane voltage (TMV) on the (a) bridging hydroxyl fraction (−$O_{br}H$), (b) oxygen-vacancy concentration (O_v), (c) specific surface area (S_A), (d) electrical conductivity (σ), (e) particle diameter (D), and (f) catalyst density (ρ). Red dashed lines represent linear fitting results. Pearson correlation coefficients (r) and coefficients of determination (R^2) are shown in each panel. Source data are provided as a Source Data file.

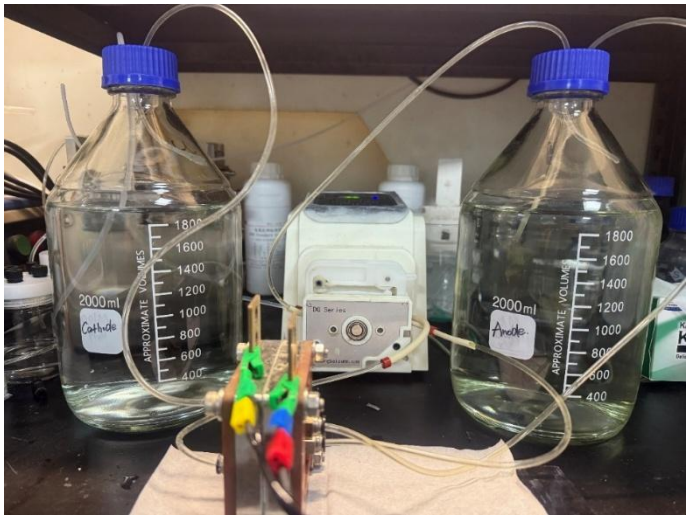

Supplementary Figure 37 | Evidence for Co_3O_4 degradation. The anolyte solution became yellowish during prolonged operation, likely due to dissolution of Co_3O_4 into the electrolyte.

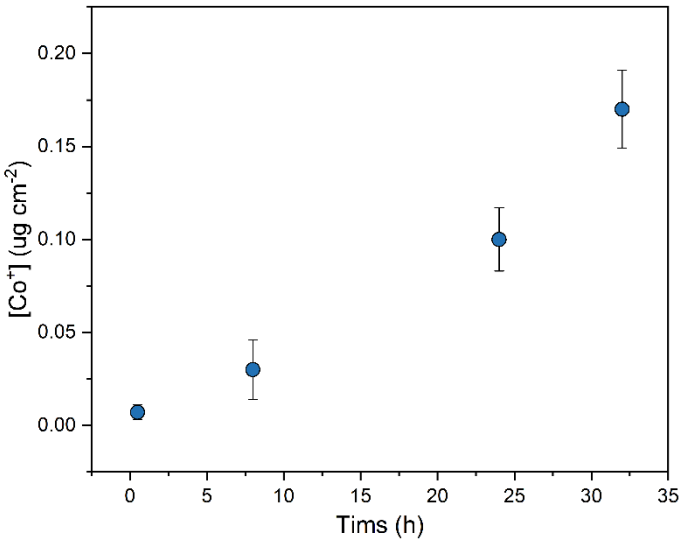

Supplementary Figure 38 | Dissolved Co quantified by ICP-OES from the electrolyte after electrochemical operation.

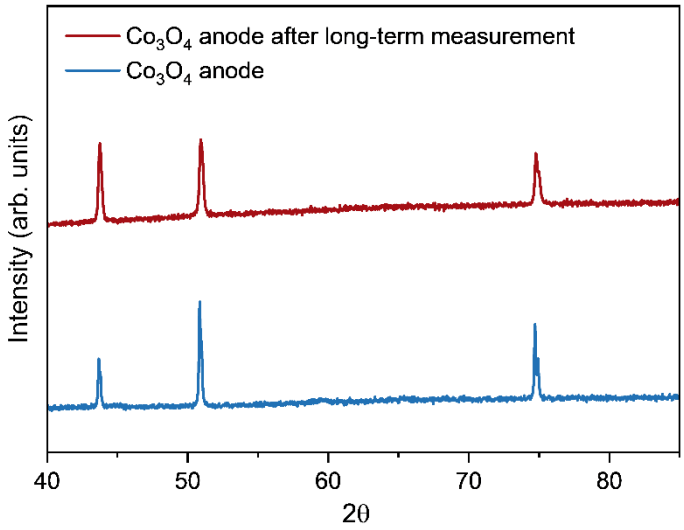

Supplementary Figure 39 | XRD patterns of the Co_3O_4 anode in the as-synthesized state and after electrochemical operation.

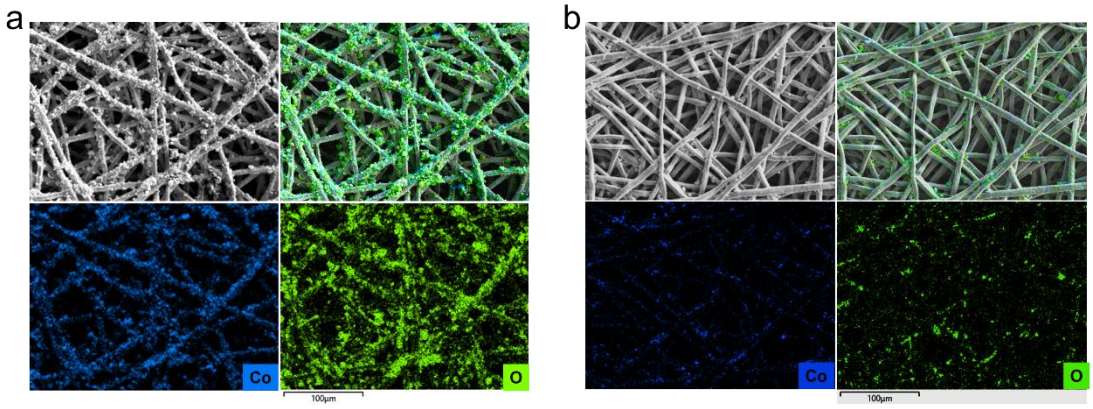

Supplementary Figure 40 | SEM images and corresponding EDS elemental mappings of the Co_3O_4 catalyst layer in the (a) as-synthesized state and (b) after long-term electrochemical operation.

Under operating conditions at 1 A cm^{-2} in pure water electrolysis, the amount of dissolved cobalt is approximately 0.10 µg cm^{-2} after 24 h. The measured Co concentration increases further with extended operation time, reaching approximately 0.17 µg cm^{-2} after 36 h, indicating a gradual loss of cobalt during prolonged electrolysis. XRD patterns recorded after long-term operation show no detectable phase transformation, confirming preservation of the spinel structure. However, SEM–EDS elemental mapping reveals a measurable decrease in cobalt content relative to the pristine electrode, consistent with partial material loss. Together, the quantitative ICP results and post-operation characterization support the conclusion that gradual Co dissolution contributes to the observed activity degradation.

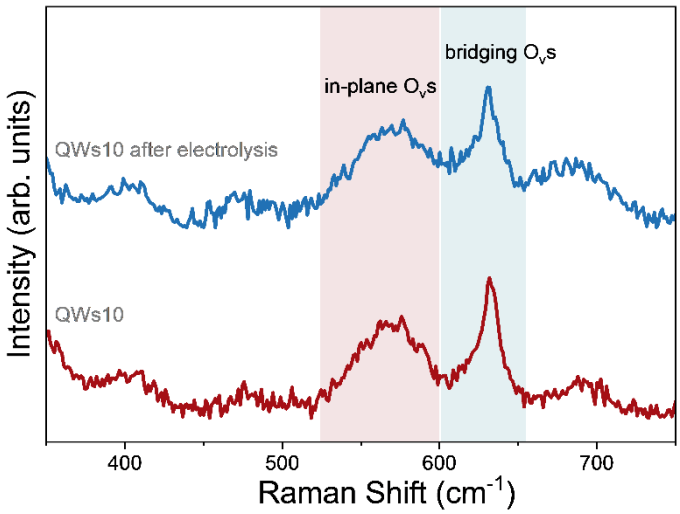

Supplementary Figure 41 | Raman spectrum of SnO_2 QWs10 recorded after 10 h electrolysis at 1 A cm^{-2}. The vacancy-related bands at ~571 cm^{-1} and ~629 cm^{-1}, assigned to in-plane and bridging oxygen vacancies, remain observable after operation, indicating the persistence of $-O_{br}H$-associated motifs.

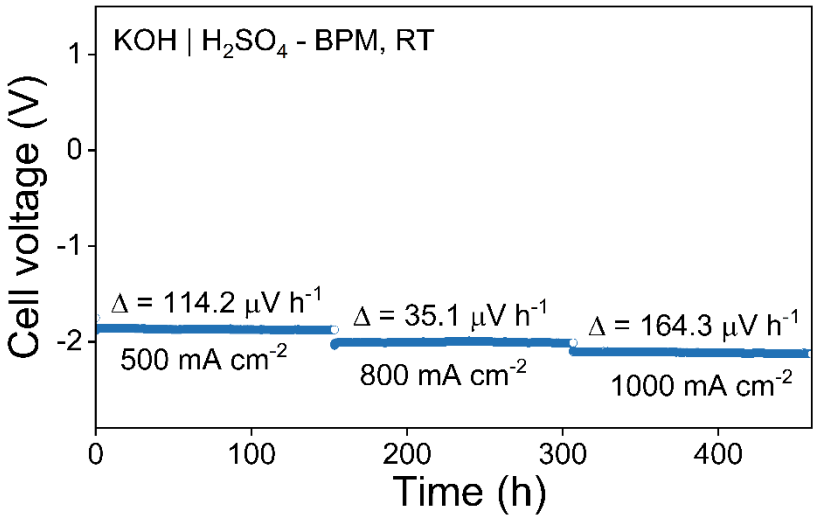

Supplementary Figure 42 | 450-h water electrolysis in the acid-base electrodialysis-like mode at room temperature (RT, 25 ºC) and current densities from 0.5 to 1 A cm^{-2}.

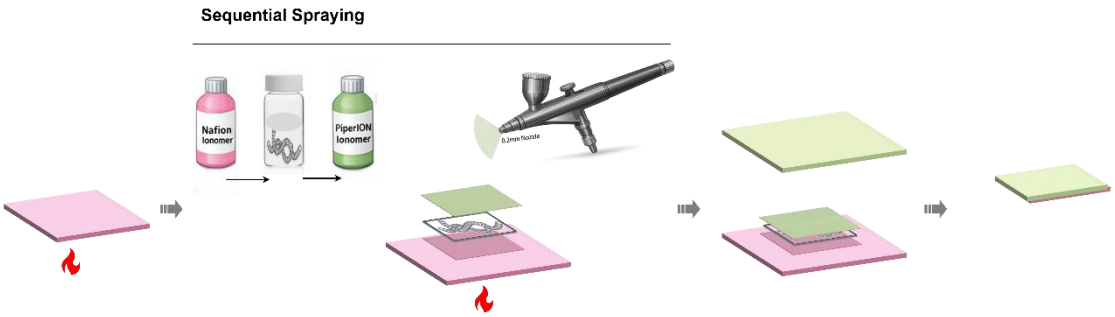

Supplementary Figure 43 | Schematic illustration of the fabrication process for BPMs.

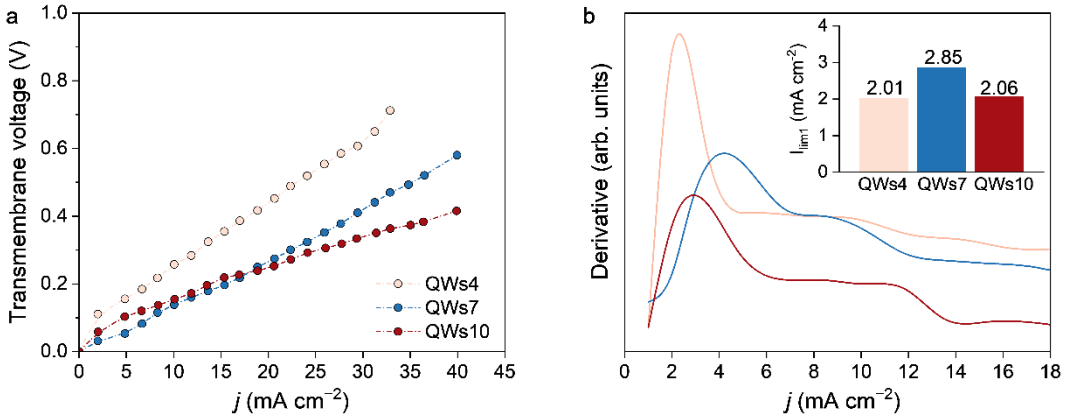

Supplementary Figure 44 | Water dissociation performance of the QWs in the kinetic-controlled regime. (a) j-V (0 ~ 50 mA cm^{-2}) and (b) corresponding derivative curves (dV/dj). The inset in b summarizes the first limiting current density (I_{lim}) extracted from the derivative analysis for QWs4, QWs7, and QWs10. Source data are provided as a Source Data file.

Supplementary Table 1. Quantification of paramagnetic superoxide species (O_2^-) in SnO_2.

Sample	QWs4	QWs7	QWs10	QWs-Ann
spins/g	9.159×10^{12}	1.092×10^{13}	1.455×10^{13}	2.016×10^{12}

Supplementary Table 2. Oxygen species analysis derived from high-resolution O 1s XPS spectra.

Sample	O_a (%)	O_v (%)	O_l (%)
QWs4	7.5	57.9	34.6
QWs7	9.0	60.9	30.1
QWs10	12.8	62.4	24.8
QWs-Ann	4.1	42.1	53.8

Supplementary Table 3. Bond length, coordination number, and disorder factor obtained by EXAFS fitting at the Sn *K*-edge.

Sample	Shell	Bond length (Å)	Coordination Number	σ^2 ($Å^2$)	E_0 shift (eV)	R-factor
SnO_2	Sn-O	2.06±0.01	6.1±0.7	0.002±0.001	5.3±1.5	0.020
	Sn-Sn	3.17±0.01	2.3±0.5	0.003±0.002		
SnO	Sn-O	2.20±0.01	3.4±0.4	0.012±0.003	8.2±1.0	0.018
	Sn-Sn	3.38±0.01	2.3±0.5	0.005±0.002		
QWs4	Sn-O	2.06±0.01	5.2±0.4	0.003±0.001	6.5±0.9	0.019
	Sn-Sn	3.19±0.01	2.0±0.5	0.002±0.001		
QWs7	Sn-O	2.05±0.01	5.1±0.3	0.003±0.001	7.3±1.0	0.014
	Sn-Sn	3.18±0.01	2.1±0.4	0.002±0.000		

Supplementary Table 4. Deconvolution of the Raman bands from 500 to 700 cm^{-1} for SnO_2 QWs.

Sample	i-O_v (%)	b-O_v (%)
QWs4	66	34
QWs7	55	45
QWs10	45	55

Supplementary Table 5. Comparison of physicochemical properties and electrochemical performance of all samples.

Sample	Type	TMV (V)	-O_{br}H/b-O_V (%)	O_v ($\times10^{12}$ spins g^{-1})	Surface area (m^2 g^{-1})	Conductivity (S m^{-1})	Diameter (nm)	Density (g cm^{-3})
QWs4	SnO_2	1.07	34	9.16	165	0.0023	1.9	6.95
QWs7	SnO_2	0.90	45	10.92	153	0.0027	2.2	6.95
QWs10	SnO_2	0.88	55	14.55	158	0.0026	3.1	6.95
QWs12	SnO_2	0.89	53	13.85	156	0.0027	4.2	6.95
QDs	SnO_2	1.79	9	5.64	193	0.0025	2.5	6.95
R-TiO_2	TiO_2	1.74	12	4.31	23	0.0005	30	4.23
H-Ann-R-TiO_2	TiO_2	1.82	2	0.11	21	0.0059	34	4.23

The −O_{br}H/b-Ov fraction is derived from Raman peak-area analysis under consistent fitting constraints. The transmembrane voltage (TMV) is measured using a membrane potential-sensing setup under identical operating conditions at a catalyst loading of 14 μg cm^{-2}. The particle diameter (D) is determined from TEM statistical analysis. The specific surface area (S) is measured by N_2 adsorption–desorption using the BET method. The electrical conductivity (σ) is obtained from bulk conductivity measurements. The density (ρ) corresponds to the intrinsic material density. The O_v concentration is quantified from EPR spectra using vacancy-associated paramagnetic electron states.

Supplementary Table 6. Comparison of the performance of BPMs and BPM electrolyzers at high current densities.

Catalyst	Current density@Cell potential/Transmembrane potential	Stability @ current density and cell degradation rate	Electrolyte	Temperature	Electrode Area	Cell Configuration	Ref
SnO_2 QWs	**1 A cm^{-2} @ 1.98 V / 0.88±0.02 V**	**550 h @ 1 A cm^{-2} and 0.87 mV h^{-1}**	**H_2O**	**60** °C	**1 cm^2**	**MEA**	**This Work**
	1 A cm^{-2} @ 1.89 V / N.A.	**450 h @ 0.5-1 A cm^{-2} and < 0.16 mV h^{-1}**	**0.5 M H_2SO_4 1 M KOH**	**60** °C	**1 cm^2**	**MEA**	
3 nm SnO_2	1 A cm^{-2} @ 2.1 V / ~0.92 V *(a)*	100 h @ 1 A cm^{-2} and 2.4 mV h^{-1} *(b)*	H_2O	55 °C	1 cm^2	MEA	*Nat. Mater.* **23**, 1421–1427 (2024)
IrO_2|NiO	0.5 A cm^{-2} @ 2.4 V /1.10 V	4 h @ 0.5 A cm^{-2} and 10 mV h^{-1}	H_2O	50 °C	4 cm^2	MEA	*Science* **369**, 1099–1103 (2020).
GO-NCA	1 A cm^{-2} @ 2.7 V / 0.92 V	400 h @ 0.5 A cm^{-2} and 2 mV h^{-1}	H_2O	80 °C	4 cm^2	MEA	*Energy Environ. Sci.* **18**, 728–737 (2025).
	1 A cm^{-2} @ 1.9 V / N.A.	90 h @ 0.1 A cm^{-2} and N.A	0.5 M H_2SO_4 1 M KOH	80 °C	4 cm^2	MEA	
SnO_2	1 A cm^{-2} @ 2.68 V / 0.95 V	1000 h @ 0.3-0.5 A cm^{-2} and 1.1 mV h^{-1}	H_2O	60 °C	4 cm^2	MEA	*Nat. Commun.* **15**, 10220 (2024).
SnO_2 @MBM	1 A cm^{-2} @ 2.3 V / 1.13 V	550 h @ 0.3 A cm^{-2} and 57.1 mV h^{-1}	0.5 M Na_2SO_4	RT	1 cm^2	Four-electrode cell	*Nat. Commun.* **14**, 1619 (2023).

CIBM	1 A cm^{-2} @ 3.95 V / 1.17 V	210 h @ 1 A cm^{-2} and 0.3 mV h^{-1}	1 M KOH with 2000 ppm KNO_3	RT	1 cm^2	Four-electrode setup	*Energy Environ Sci.* **16**, 3815–3824 (2023).
TiO_2	0.5 A cm^{-2} @ 2.6 V / N.A.	N.A.	N.A.	N.A.	N.A.	MEA	*Joule* **7**, 765–781 (2023).
	0.5 A cm^{-2} @ 3.6 V / N.A.	20 h @ 0.25 A cm^{-2} and 23.3 mV h^{-1}	Seawater	50 °C	1 cm^2	MEA	
TiO_2-P25	0.5 A cm^{-2} @ 2.05 V / N.A.	N.A.		55 °C	1 cm^2	MEA	*Nat. Commun.* **13**, 3846 (2022)
IrO_X	0.5 A cm^{-2} @ 1.95 V / N.A.			55 °C	1 cm^2	MEA	

Note: [(a)] The value of η_{WD} = 100±20 mV, together with an equilibrium potential of approximately 0.82 V, yields an estimated transmembrane potential of around 0.92 V. [(b)] The degradation rate of 2.4 mV h^{-1} was derived from its original full-cell voltage stability data. N.A. indicates that the result is not available.

Supplementary Table 7. The information on the anion- and cation-exchange layers.

Membrane	**Thickness (μm)**	**Ultimate Tensile Strength-Max (MPa)**	**IEC (H^+ or OH^-)**	**Conductivity (mS cm^{-1}, 80 °C)**	**Water Uptake (%)**	**Swelling Ratio (%)**
Nafion NR211 (CEL)	25	23 (MD) 28 (TD)	0.92 (H^+, meq/g)	100 (100% RH)	5.0±3.0%	50±5%
PiperION-A20-HCO_3 (AEL)	20	> 30	2.35 (OH^-, meq/g)	150 (OH^-)	8.0±3.0%	50 (80 ℃ in 1M KOH)

Supplementary References:

1. Anpo, M. *et al.* Generation of superoxide ions at oxide surfaces. *Top. Catal.* **8**, 189–198 (1999).
2. Wang, C. *et al.* Proton Conduction Mechanism on Hydrated SnO_2 Nanoparticles: Impedance Spectroscopy and Nuclear Magnetic Resonance Analysis. *J. Phys. Chem. C* **128**, 11410–11418 (2024).
3. Zhou, C. *et al.* Proximity-independent acid–base synergy in a solid ZrO_xH_y catalyst for amine regeneration in post-combustion CO_2 capture. *Nat. Catal.* **8**, 270–281 (2025).
4. Chen, J. *et al.* Interactions of Oxide Surfaces with Water Revealed with Solid-State NMR Spectroscopy. *J. Am. Chem. Soc.* **142**, 11173–11182 (2020).